

# Asteroseismic detection of a predominantly toroidal magnetic field in the deep interior of the main-sequence F star KIC 9244992

Masao Takata,<sup>1★</sup> Simon J. Murphy,<sup>2†</sup> Donald W. Kurtz,<sup>3,4</sup> Hideyuki Saio<sup>5</sup> and Hiromoto Shibahashi<sup>1</sup>

<sup>1</sup>Department of Astronomy, School of Science, The University of Tokyo, 7-3-1 Hongo, Bunkyo-ku, Tokyo 113-0033, Japan

<sup>2</sup>Centre for Astrophysics, University of Southern Queensland, Toowoomba, QLD 4350, Australia

<sup>3</sup>Centre for Space Research, North-West University, Dr Albert Luthuli Drive, Mahikeng 2735, South Africa

<sup>4</sup>Jeremiah Horrocks Institute, University of Lancashire, Preston, PR2 2HE, UK

<sup>5</sup>Astronomical Institute, Graduate School of Science, Tohoku University, Sendai, Miyagi 980-8578, Japan

Accepted 2025 November 28. Received 2025 October 17; in original form 2025 August 15

## ABSTRACT

An asteroseismic analysis has revealed a magnetic field in the deep interior of a slowly-rotating main-sequence F star KIC 9244992, which was observed by the *Kepler* spacecraft for four years. The star shows clear asymmetry of frequency splittings of high-order dipolar gravity modes, which cannot be explained by rotation alone, but are fully consistent with a model with rotation, a magnetic field and a discontinuous structure (glitch). Careful examination of the frequency dependence of the asymmetry allows us to put constraints on not only the radial component of the magnetic field, but also its azimuthal (toroidal) component. The lower bounds of the root-mean-squares of the radial and azimuthal components in the radiative region within 50 per cent in radius, which have the highest sensitivity in the layers just outside the convective core with a steep gradient of chemical compositions, are estimated to be  $B_r^{\min} = 3.5 \pm 0.1$  kG and  $B_\phi^{\min} = 92 \pm 7$  kG, respectively. The much stronger azimuthal component than the radial one is consistent with the significant contribution of the differential rotation although the star has almost uniform rotation at present. The estimated field strengths are too strong to be explained by dynamo mechanisms in the radiative zone associated with the magnetic Tayler instability. The aspherical glitch is found to be located in the innermost radiative layers where there is a steep gradient of chemical composition. The first detection of magnetic fields in the deep interior of a main-sequence star sheds new light on the problem of stellar magnetism, for which there remain many uncertainties.

**Key words:** asteroseismology – stars: individual: KIC 9244992 – stars: interiors – stars: magnetic field – stars: oscillations – stars: variables: general

## 1 INTRODUCTION

The study of magnetic fields in stars has been a major subject in astrophysics since Hale (1908) first detected them in sunspots. The Sun has not only strong magnetic fields of the order of  $10^3$  G confined in sunspots but also a global-scale weak field of the order of 1 G, which extends from the photosphere to the corona. The number of sunspots (Schwabe 1844) and their latitudinal position (Spörer’s law; Carrington 1863) both change over a period of about eleven years, which actually corresponds to a half of the magnetic cycle of about twenty-two years (Hale et al. 1919). Understanding the mechanism of how the magnetic fields are generated and maintained is the central problem of the activity of the Sun and low-mass main-sequence stars (e.g. Hathaway 2015).

On the other hand, large-scale nearly dipolar magnetic fields with typical strengths of  $10^3$  G are detected at the surface of a small fraction of early-type main-sequence stars that do not have a thick convective envelope (Landstreet 1982). In early studies Babcock (1947) first reported the detection of magnetic fields mainly in A and B type stars

with chemical peculiarities, whereas recent surveys have extended the detections to O and B type stars (e.g. Briquet 2015; Wade et al. 2016; Shultz et al. 2019; Petit & Oksala 2025). Unlike the Sun, these fields are apparently stable (at least on human observation time scales), and their observed variability is interpreted as rotational modulation with the magnetic axis inclined to the rotation axis (Stibbs 1950). These fields could originate from interstellar fields that were locked into the stars during the formation process (Borra et al. 1982). Or they might alternatively come from the dynamo process in the stars (Stepień 2000).

We now give an overview of the surface fields of pulsating main-sequence stars with low and intermediate mass. The first example of magnetic pulsators is the rapidly oscillating Ap (roAp) stars (Kurtz 1982, 1990), which show high-order acoustic modes with a typical periods around 10 min under significant influence of the surface field of the order of  $10^3$  G. Although the roAp stars are found in the same region in the HR diagram as  $\delta$  Sct stars, which show only low to intermediate order modes, the large-scale strong surface magnetic field has long been thought to be incompatible with low-order oscillation modes.

This situation changed when surface fields were detected in a

★ E-mail: takata@astron.s.u-tokyo.ac.jp (MT)

† E-mail: simon.murphy@usq.edu.au (SJM)

few  $\delta$  Sct stars (Thomson-Paressant et al. 2023), and when Murphy et al. (2020) discovered the first example of  $\delta$  Sct–roAp hybrid stars, KIC 11296437, with the surface field of  $2.8 \pm 0.5$  kG. Furthermore, Murphy et al. argued, based on theoretical analysis, that strong surface fields could inhibit high-order gravity modes. In fact, there has so far been no detection of a large-scale surface magnetic field in  $\gamma$  Dor stars and  $\delta$  Sct– $\gamma$  Dor hybrid pulsators (e.g. Thomson-Paressant et al. 2023; Hubrig et al. 2023). However, the hypothesis of suppression of high-order gravity modes by strong magnetic fields must be examined quantitatively because surface magnetic fields and high-order gravity modes do coexist in slowly pulsating B (SPB) and SPB– $\beta$  Cep hybrid stars (e.g. Neiner et al. 2003; Briquet et al. 2013), which are also main-sequence stars, but with higher masses ( $3\text{--}9 M_{\odot}$ ) than  $\gamma$  Dor stars. In this context, we note that the low-frequency peak found in the spectrum of some  $\gamma$  Dor stars may be caused by surface spots, which are associated with small-scale surface magnetic activity (Henriksen et al. 2023b,a; Antoci et al. 2025). In summary, thanks to improvements in observational techniques, the number of confirmed main-sequence magnetic pulsators is steadily increasing. This naturally leads to a stronger motivation to understand these stars also from a theoretical point of view.

The surface magnetic fields are detected not only in main-sequence stars, but also in stars in the initial (pre-main-sequence) stage of their lives (T Tauri stars) and those in the final stage (white dwarfs and neutron stars) (e.g. Bagnulo & Landstreet 2021). The magnetic fields thus play significant roles throughout the entire life of stars affecting many physical processes, including star formation, rotation, mass accretion, flares and winds (e.g. Mestel 2012).

While surface magnetic fields are measured by the Zeeman effect of spectral lines, asteroseismology provides a unique method to constrain the internal magnetic fields through their effect on stellar oscillations. Among others, Li et al. (2022) have carefully examined the oscillation frequencies of three red-giant stars, which were observed by the *Kepler* spacecraft, to deduce the detection of fields of  $30\text{--}100$  kG in the core. This analysis has been extended to a larger sample of stars by Deheuvels et al. (2023), Li et al. (2023) and Hatt et al. (2024).

Turning to main-sequence stars, Lecoanet et al. (2022) estimated an upper limit of the magnetic-field strength in the near-core region of the main-sequence B star HD 43317 to be of order 500 kG. This was based on the picture that the observed suppression of gravity modes in the low-frequency range is due to the conversion of constituent waves from the internal gravity waves to resonant Alfvén waves as a result of significant interaction with the magnetic field in the layer of the steep gradient of chemical composition just outside the convective core (Lecoanet et al. 2017). The essential part of this picture was originally presented by Fuller et al. (2015) to explain unusually low amplitudes of dipolar modes in a fraction of red-giant stars observed by the *Kepler* space telescope (Mosser et al. 2012; García et al. 2014). However, Mosser et al. (2017) contradicted this idea by demonstrating that the low-amplitude dipolar modes of red giants are formed by the coupling between core and envelope oscillations, which implies that the waves transmitted from the envelope to the core come back to the envelope (at least partially). This is not expected by the mechanism of Fuller et al. (2015), at least in its original form. Continuing efforts have been made to understand the mechanism of mode suppression and its relation to the magnetic field from both observational aspects (e.g. Stello et al. 2016; Coppée et al. 2024) and theoretical ones (e.g. Loi 2020; Rui & Fuller 2023).

Following recent work on red-giant stars, we report in this paper the detection of a magnetic field in the deep interior of a main-sequence F star, KIC 9244992, which can be classified as a  $\delta$  Sct– $\gamma$  Dor hybrid

**Table 1.** Parameters for KIC 9244992 from Brown et al. (2011) (B11), Huber et al. (2014) (H14) and Nemec et al. (2017) (N17).

Parameter	Value	Reference
Kepler magnitude (mag)	13.998	B11
$T_{\text{eff}}$ (K)	$6900 \pm 292$	H14
	$7550 \pm 100$	N17
$\log g$ (cgs)	$3.52 \pm 0.40$	H14
	$3.52 \pm 0.15$	N17
$v \sin i$ ( $\text{km s}^{-1}$ )	$< 6 \pm 1$	N17
[Fe/H]	$-0.15 \pm 0.30$	H14
	$+0.1 \pm 0.3$	N17

pulsator (Saio et al. 2015, hereafter S15). The structure of this paper is as follows: the main analysis is presented in Section 2 with the details given in Appendices; Section 3 is devoted to discussions; we finally give conclusions in Section 4.

## 2 ASYMMETRY OF FREQUENCY SPLITTINGS

### 2.1 Target

KIC 9244992 has a *Kepler* magnitude of  $K_p = 14$  (Brown et al. 2011) and a spectral type of F0 (Nemec et al. 2017). There is no observational evidence that the star belongs to a binary (or multiple) system (Murphy et al. 2018). The properties of the star are summarised in Table 1.

S15 analysed the *Kepler* long cadence data of the star in quarters 1 to 17 to find rich frequency spectra of both of gravity and acoustic modes. Using the MESA stellar evolution code (Paxton et al. 2011, 2013, 2015, 2018, 2019; Jermyn et al. 2023), they then constructed evolutionary models, which reproduce the observed properties well. The best model has a mass of  $1.45 M_{\odot}$ , an initial metal abundance of  $Z_0 = 0.01$  and an age of 1.9 Gyr, which implies the late phase of the main-sequence stage (see Table 2). From the observed frequency splittings, they estimated the rotation periods of the core and the envelope to be  $63.51 \pm 0.28$  d and  $66.18 \pm 0.58$  d, respectively.

The star can be classified as a  $\delta$  Sct– $\gamma$  Dor hybrid pulsator, though its rotation period is much longer than the typical value of  $\sim 1$  d of  $\gamma$  Dor stars (Li et al. 2020). Most stars rotating this slowly with this  $T_{\text{eff}}$ ,  $\log g$ , and age show Am chemical peculiarities, or Ap peculiarities if there is a surface magnetic field. A high-resolution spectroscopic study of KIC 9244992 would be useful to examine its surface abundances.

### 2.2 Measurement

While the internal rotation can be inferred from the difference between the lowest frequency and highest frequency of each g-mode triplet (e.g. Aerts et al. 2010), we may study magnetic fields and the second-order effect of rotation based on the asymmetry of triplets, which is defined by

$$\alpha_n \equiv \frac{\nu_{n,1,1} + \nu_{n,1,-1}}{2} - \nu_{n,1,0}. \quad (1)$$

Here,  $\nu_{n,\ell,m}$  generally represent mode frequencies with radial order  $n$ , spherical degree  $\ell$  and azimuthal order  $m$ .

In Fig. 1, we plot  $\alpha_n$  as a function of  $\nu_{n,1,0}$  for all of the seventeen gravity-mode triplets between  $0.9 \text{ d}^{-1}$  and  $1.8 \text{ d}^{-1}$ , whose frequencies are listed in Table 1 of S15. The first point we should note is that all  $\alpha_n$  except those at  $1.29 \text{ d}^{-1}$ ,  $1.70 \text{ d}^{-1}$  and  $1.78 \text{ d}^{-1}$  are statistically

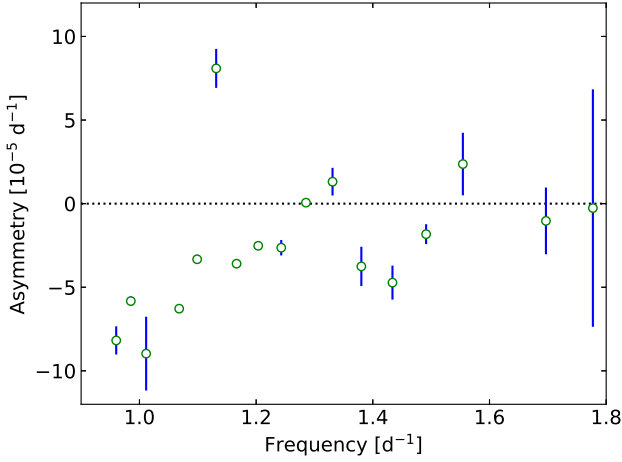


**Figure 1.** Asymmetry of frequency splittings  $a_n$  (see equation 1) for high-order gravity modes in KIC 9244992. Errors are smaller than the symbol size for the points without error bars.

significantly different from zero, although all  $|a_n|$  are smaller than the frequency resolution,

$$f_{\text{res}} = \frac{1}{4T_0} = 1.7 \times 10^{-4} \text{ d}^{-1} \quad (2)$$

(Kallinger et al. 2008), where  $T_0 = 1459 \text{ d}$  is the total observation time-span of the *Kepler* primary mission Q1–17 data for KIC 9244992. The pulsation frequencies can be determined to higher precision than the frequency resolution, so long as there are no undetected, unresolved frequencies within the spectral window of the mode frequency peaks. The consistency of our results for  $a_n$  indicates that this is the case. Given that, we list the following properties of  $a_n$ : (1) a negative and decreasing trend below  $1.25 \text{ d}^{-1}$ ; (2) pseudo-sinusoidal behaviour, particularly for  $\nu \gtrsim 1.3 \text{ d}^{-1}$ , with a wavelength of several data points; (3) an outlier at  $1.13 \text{ d}^{-1}$ . The main question of this paper is how we can understand these.

### 2.3 Theory

In the present analysis, we assume that asymmetry of the frequency splitting arises from the three effects,

$$a_n = a_n^{(\text{rot})} + a_n^{(\text{mag})} + a_n^{(\text{glitch})}, \quad (3)$$

in which  $a_n^{(\text{rot})}$ ,  $a_n^{(\text{mag})}$  and  $a_n^{(\text{glitch})}$  indicate the effects of rotation, a magnetic field and a discontinuous structure (glitch), respectively. There are three remarks about equation (3): First, we assume that the first-order effect of rotation is much larger than that of the magnetic field. In fact, Table 1 of S15 shows that the frequency splittings are all equal to about  $8 \times 10^{-3} \text{ d}^{-1}$ , which is larger by two orders of magnitude than the observed asymmetry in Fig. 1. However, since the rotational splitting is symmetric, the first-order effect of rotation cannot influence  $a_n$  and we need to analyse its second-order effect. Second, in contrast, it is sufficient to consider the first-order effects for the magnetic field and the glitch. Finally, we assume that the deformation of the equilibrium structure caused by the Lorentz force is negligible compared to that caused by the centrifugal force. We will discuss this assumption at the end of Section 2.5.

Each of the three terms on the right-hand-side of equation (3) is discussed separately in the following subsections.

#### 2.3.1 Rotation effect

For simplicity, we restrict ourselves to the case of uniform rotation (without the magnetic field), which is a good approximation for KIC 9244992 (see Section 2.1). From a physical point of view, the second-order effect of rotation is composed of two sources (in the Eulerian picture), the second-order effect of the Coriolis force, which directly affects the oscillations, and the deformation of the equilibrium structure due to the centrifugal force.

Although we need to rely on sophisticated methods and stellar models to quantify the corresponding  $a_n^{(\text{rot})}$  accurately, it would be worth providing a model-independent analytical formula for the order-of-magnitude estimates. For high-order gravity modes, the Coriolis force becomes more important than the centrifugal force, because the former effect is inversely proportional to the frequency (the ratio between the Coriolis force and the acceleration of the oscillation). Using equation (117) of Dziembowski & Goode (1992) (see also Brassard et al. 1989), we estimate for dipolar modes ( $\ell = 1$ ),

$$a_n^{(\text{rot,asympt})} \equiv \frac{\nu_{\text{rot}}^2}{40\nu_{n,1}} \quad \text{as } \nu_{n,1} \rightarrow 0, \quad (4)$$

in which  $\nu_{\text{rot}}$  means the (cyclic) rotation frequency. Equation (4) can be rewritten as

$$a_n^{(\text{rot,asympt})} = 6 \times 10^{-6} \left( \frac{P_{\text{rot}}}{64 \text{ d}} \right)^{-2} \left( \frac{\nu_{n,1}}{1 \text{ d}^{-1}} \right)^{-1} \text{ d}^{-1}, \quad (5)$$

where  $P_{\text{rot}} = \nu_{\text{rot}}^{-1}$  means the rotation period. The rotation effect is opposite in sign to and smaller in amplitude by an order of magnitude than the observed asymmetry in Fig. 1. We conclude that there exist some physical effects other than the rotation in the star.

#### 2.3.2 Magnetic effect

The frequency change due to a weak magnetic field is analysed in the framework of the regular perturbation theory (e.g. Gough & Thompson 1990; Shibahashi & Takata 1993). Analyses that can be adapted to the case of high-order and low-degree gravity modes have been developed in some recent papers (e.g. Mathis et al. 2021; Li et al. 2022). We extend these previous works under the assumption of  $|B_\phi| \gg |B_r|, |B_\theta|$ , where  $B_r$ ,  $B_\theta$  and  $B_\phi$  represent  $r$ ,  $\theta$  and  $\phi$  components of the magnetic field in the spherical coordinates (with the rotation axis in the direction of  $\theta = 0$ ), respectively. The reason for dominant  $B_\phi$  is that this component could easily be increased by rotation ( $\Omega$  effect). In order to define the  $\phi$  component, it is necessary to identify a magnetic axis. Although we assume that this magnetic axis is aligned with the rotation axis, this does not necessarily mean that the field is axisymmetric. Namely, each component can generally depend on  $\phi$ . (Still, we may note that Gauss's law for magnetism ( $\nabla \cdot \mathbf{B} = 0$ ) leads to  $|\partial B_\phi / \partial \phi| \ll |B_\phi|$ , which implies approximate axisymmetry.) The motivation of this extension comes from the fact that the asymmetry in Fig. 1 does not perfectly follow the inverse-cube law of frequency (e.g. Bugnet et al. 2021). In fact, we show in appendix A (equation (A67)) that the asymmetry of frequency splittings is given as a function of the unperturbed frequency  $\nu_{n,1}$  by

$$a_n^{(\text{mag})} = \frac{a}{\nu_{n,1}^3} + \frac{b}{\nu_{n,1}}, \quad (6)$$

in which frequency-independent parameters  $a$  and  $b$  are given by

$$a = S_r \langle W_r B_r^2 \rangle \quad (7)$$

and

$$b = S_h \langle W_\phi B_\phi^2 \rangle, \quad (8)$$

respectively. Here,  $S_r$  and  $S_h$  represent the sensitivity to the equilibrium structure, defined in terms of the density  $\rho$  and the Brunt-Väisälä frequency  $N$  by

$$S_r \equiv \frac{3}{128\pi^5} \frac{\int_{G_B} \frac{N^3}{\rho r^3} dr}{\int_G \frac{N}{r} dr}, \quad (9)$$

and

$$S_h \equiv -\frac{9}{32\pi^3} \frac{\int_{G_B} \frac{N}{\rho r^3} dr}{\int_G \frac{N}{r} dr}, \quad (10)$$

respectively. The domains of the radial integral  $G$  and  $G_B$  respectively mean the gravity-mode cavity and its subdomain where the magnetic field exists. The gravity-mode cavity  $G$  extends to almost the entire radiative region in the case of intermediate-mass main-sequence stars. The angle brackets in equations (7) and (8) stand for the volume average over  $G_B$ , which is defined by

$$\langle W_\alpha B_\alpha^2 \rangle \equiv \int_{G_B} K_\alpha(r) \overline{W_\alpha B_\alpha^2} dr \quad \text{for } \alpha = r \text{ and } \phi, \quad (11)$$

with the spherical average introduced by

$$\overline{W_\alpha B_\alpha^2} \equiv \frac{1}{4\pi} \int_{4\pi} B_\alpha^2(r, \theta, \phi) W_\alpha(\cos \theta) \sin \theta d\theta d\phi. \quad (12)$$

The kernels in the radial direction are defined by

$$K_r(r) \equiv \left( \int_{G_B} \frac{N^3}{\rho r^3} dr \right)^{-1} \frac{N^3}{\rho r^3} \quad (13)$$

and

$$K_\phi(r) \equiv \left( \int_{G_B} \frac{N}{\rho r^3} dr \right)^{-1} \frac{N}{\rho r^3}. \quad (14)$$

As examples, the profiles of  $K_r$  and  $K_\phi$  are plotted in Fig. 2 for the best model with the upper limits of  $G_B$  set at 50 per cent of the total radius. The upper limits should be carefully fixed to be consistent with the assumptions of the analysis (see Section 2.5). While the amplitude of  $K_r$  concentrates on the sharp peak around  $r = 0.06R$ , which corresponds to the layers of a steep gradient in mean molecular weight,  $K_\phi$  not only takes a local maximum at the same position as  $K_r$ , but also has a long tail towards larger  $r$ . The difference is because  $K_r$  depends on a higher power of  $N$  than  $K_\phi$ . On the other hand, the weight functions for the spherical averages are introduced by

$$W_r(\cos \theta) \equiv P_2(\cos \theta) = \frac{3 \cos^2 \theta - 1}{2}, \quad (15)$$

and

$$W_\phi(\cos \theta) \equiv \frac{5 \cos^2 \theta - 1}{4}. \quad (16)$$

In equation (15), function  $P_2$  is the Legendre polynomial of degree two.

We have made no assumption about the ratio between the two terms on the right-hand side of equation (6). Therefore, the second term can in principle dominate over the first term, when  $|B_\phi|$  is much larger than  $|B_r|$ . In this case, the asymmetry would be proportional to the inverse of frequency, rather than the inverse cube.

The difference between the two terms on the right-hand side of equation (6) can be understood from a physical point of view. Since the oscillation motion is predominantly horizontal for high-order

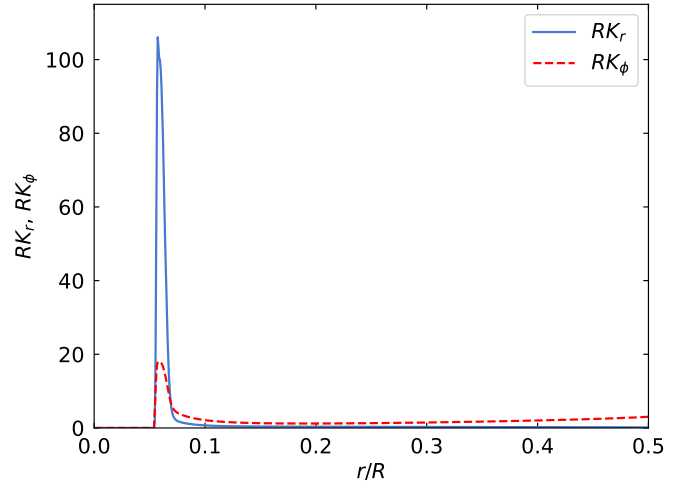


**Figure 2.** Profiles of  $K_r$  (solid curve) and  $K_\phi$  (dashed curve) multiplied by the total radius  $R$  for the best evolutionary model (model A in Table 2) with the upper limit of  $G_B$  set at 50 per cent of the total radius. The gradual increase of  $RK_\phi$  towards larger  $r/R$  actually complicates the interpretation, which is treated in Section 2.5 in detail.

gravity modes, the magnetic field in the radial direction would be significantly bent by the short-wavelength motions to generate a strong restoring Lorentz force. On the other hand, the field in the azimuthal direction is nearly parallel to the motion for  $\ell = 1$  and  $m = \pm 1$  modes near the equator, where the oscillation amplitude is largest, so that there is little restoring force. For the axisymmetric modes ( $m = 0$ ), the motion is perpendicular to the azimuthal field, which means that we may expect some Lorentz force to restore the motion. However, since the wavelength in the horizontal direction is on the order of the stellar radius, which is much larger than that in the radial direction, the size of the restoring force would be much smaller than in the case of the radial field. Thus, the radial field influences the high-order and low-degree gravity modes much more significantly than the azimuthal field. This qualitatively explains why we observe  $|S_r| \gg \nu^2 |S_h|$  for  $\nu = 1 \text{ d}^{-1}$  (see the last two lines of Table 2), which implies that the first term is much larger than the second term if  $|B_r| \sim |B_\phi|$ . In addition, as the radial wavelength gets shorter for higher-order (smaller-frequency) gravity modes, the radial field is accordingly bent with the shorter scale, which results in a larger restoring Lorentz force, and hence a more significant impact on the oscillation frequencies. This is the reason for the strong frequency dependence of the first term. In contrast, the effect of the azimuthal field would depend little on the order of modes, because the bending scale of the field line in the horizontal direction is not affected by the radial wavelength. This implies a weaker frequency dependence of the second term. In fact, the inverse dependence on  $\nu_{n,1}$  originates from the perturbation to  $\nu^2$ , so that we may regard that the impact of the azimuthal field is essentially independent of the frequency if it is measured by the perturbation to the squared frequency.

### 2.3.3 Glitch effect

In Fig. 1, we observe that the data points are not distributed randomly, nor do they follow a linear trend, but instead they show correlation, which in the high-frequency range is pseudo-sinusoidal with a wavelength of several points. This is a typical signature of discontinuous structure (glitch) in the star, which disturbs the wave propagation. Because  $a_n$  is not sensitive to any spherically symmetric structure,



**Table 2.** Properties of evolutionary models by S15. Symbols  $X_c$ ,  $h_{ov}$  and  $\Pi_1$  stand for the central hydrogen abundance, the parameter of overshooting from the convective core and the period spacing of dipolar gravity modes, respectively, while  $S_r$  and  $S_h$  are defined by equations (9) and (10), respectively. The upper limit of  $G_B$  (the magnetic region in the gravity-mode cavity) is expressed by  $x_{up}$ , which is measured in units of the fractional radius. The other symbols have their usual meanings.

Model	A*	B	C
$M/M_\odot$	1.45	1.50	1.54
$T_{eff}$ (K)	6625	6748	7221
$\log L/L_\odot$	0.854	0.907	1.050
$\log R/R_\odot$	0.309	0.319	0.331
$\log g$ (cgs)	3.982	3.977	3.962
Age (Gyr)	1.9	1.7	1.4
$X_c$	0.149	0.142	0.111
$X_0$	0.724	0.724	0.727
$Y_0$	0.266	0.266	0.266
$Z_0$	0.010	0.010	0.007
$h_{ov}$	0.005	0.000	0.005
$\Pi_1$ (s)	2349	2335	2306
for $x_{up} = 0.5$			
$S_r$ ( $10^{-31} \text{ cm g}^{-1} \text{ s}^{-2}$ )	3.0	2.8	2.9
$S_h$ ( $10^{-24} \text{ cm g}^{-1}$ )	-2.5	-2.4	-2.4

Note: A\* indicates our best model (see S15).

which is usually assumed in the literature about glitches, we formulate a framework to analyse aspherical glitches in Appendix B. The glitches generally induce oscillatory structures in the diagram of period and period difference with a constant wavelength, but varying amplitude. Such a component can actually be identified in Fig. 1 based on the detailed analysis in Sections 2.4.3 and 2.4.4. While the wavelength provides us with the information about the location of each glitch, the amplitude modulation depends on the type of discontinuity. We demonstrate in Appendix B4 that the amplitude depends on the period linearly, constantly or reciprocally, if the discontinuity is associated with the density itself, its first derivative or its second derivative, respectively. We will carefully examine the type of discontinuity during our data analysis (Section 2.4.3).

## 2.4 Interpretation

### 2.4.1 Evolutionary models

We use three evolutionary models A, B and C of KIC 9244992, which are constructed by S15, to interpret the observed asymmetry of frequency splittings. The properties of the models are summarised in Table 2. Their main differences are found in mass  $M$ , initial metal abundance  $Z_0$  and parameter  $h_{ov}$  of the convective overshooting. Model A corresponds to the best model, which reproduces the observed frequencies most accurately, while the other two models also have quite close frequencies (see Fig. 11 of S15).

### 2.4.2 Rotation effect

There exist two different methods to analyse the second-order rotation effect. One is based on perturbation theory (e.g. Saio 1981; Gough & Thompson 1990; Dziembowski & Goode 1992), while the other relies on two-dimensional numerical computation (e.g. Lee & Baraffe 1995). We try both methods.

We first calculate the effect for the modes of the best evolutionary model by S15 (Section 2.1). We set the rotation period to  $P_{rot} = 64$  d,

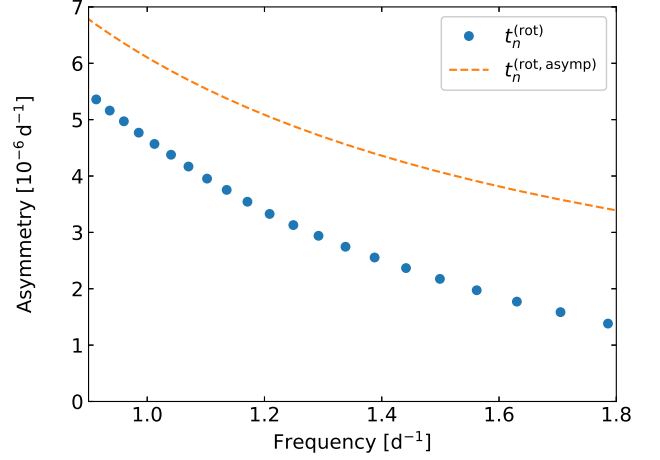


**Figure 3.** Asymmetry of frequency splittings caused by the second-order effect of rotation for the modes of our best evolutionary model (model A in Table 2). The total effects  $a_n^{(rot)}$  and the asymptotic estimates  $a_n^{(rot,asympt)}$  (see equation (4)) are shown by the filled dots and the dashed curve, respectively.

which corresponds to  $\nu_{rot} = 0.0156 \text{ d}^{-1}$ . Fig. 3 shows  $a_n^{(rot)}$  and  $a_n^{(rot,asympt)}$  (equation (4)) for the modes in the observed frequency range in Fig. 1. We have checked that the values of  $a_n^{(rot)}$ , which are estimated based on perturbation theory (Saio 1981), are consistent with a two-dimensional calculation by the program of Lee & Baraffe (1995) within one per cent. This reconfirms the conclusion of Section 2.3.1 that the observed asymmetry cannot be explained only by the rotation. Fig. 3 also demonstrates that the asymptotic formula (equation (4)) overestimates the true values by only a factor of three at most, which is acceptable for order-of-magnitude estimates.

We also calculate  $a_n^{(rot)}$  for two other evolutionary models with masses of  $1.50 M_\odot$  and  $1.54 M_\odot$ , which are shown in Fig. 13 of S15, and confirm that there is no essential difference from the case of the best model.

### 2.4.3 Type of the glitch

Given the estimates for  $a_n^{(rot)}$  based on the evolutionary models, we may interpret the remaining contribution to the observed asymmetry  $a_n$  as the combined effects of a magnetic field and a glitch. While the magnetic effects can be described by equation (6), we first need to decide which formula to use for the glitch signature.

For this purpose, we first fit equation (6) to  $a_n - a_n^{(rot)}$  in the low-frequency range between  $0.95 \text{ d}^{-1}$  and  $1.25 \text{ d}^{-1}$  (without the outlier at  $1.13 \text{ d}^{-1}$ ), where the pseudo-sinusoidal component has only a small amplitude (see Fig. 1). Then, using the fitted parameters  $a$  and  $b$ , we extract the magnetic contribution from  $a_n - a_n^{(rot)}$  in the whole range between  $0.95 \text{ d}^{-1}$  and  $1.8 \text{ d}^{-1}$ . The residuals are shown as a function of period in Fig. 4. As shown by the solid curve, we confirm that these residuals can be explained by a sinusoidal function with a constant amplitude, except for one data point at  $0.83 \text{ d}$ . The sinusoidal variation is expected for a glitch associated with the discontinuity in the first derivative of density (see Appendix B4).

After the preliminary steps to determine the type of the glitch, global fitting in the whole frequency range should be performed

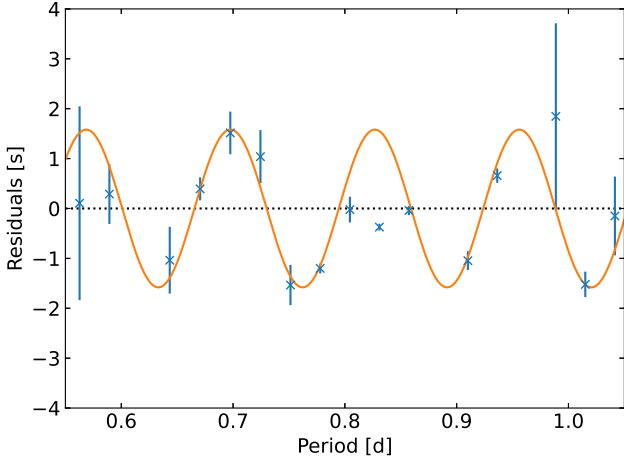


**Figure 4.** Residuals of the fitting in period,  $-\nu_{n,1}^{-2} (\alpha_n - \alpha_n^{(\text{rot})} - \alpha_n^{(\text{mag})})$ , as a function of the mode period. The fitting is performed based on equation (6) for model A (see Table 4) using only the eight modes with periods longer than 0.8 d. The residuals are computed for not only those modes but also the modes with shorter periods. The solid curve represents the best fit to the residuals by a sinusoidal function of constant amplitude, neglecting the data point at 0.83 d. There is another rejected point at 0.88 d, whose ordinate is outside the plot range. This corresponds to the outlier at  $1.13 \text{ d}^{-1}$  in Fig. 1 (see Section 3.1).

using simultaneously equation (6) and

$$\alpha_n^{(\text{glitch})} = \mathcal{A} \nu_{n,1}^2 \sin \left[ 2\pi \left( \frac{\mathcal{K}}{\nu_{n,1}} - \psi \right) \right] \quad (17)$$

(see equation (B22)), in which  $\mathcal{A}$ ,  $\mathcal{K}$  and  $\psi$  are constant parameters to be fixed.

Equation (17) suffers from two types of degeneracy. First, the expression is invariant under the transformation of

$$(\mathcal{A}, \psi) \rightarrow \left( -\mathcal{A}, \psi + \frac{1}{2} + k \right), \quad (18)$$

in which  $k$  is an arbitrary integer. Second, since the mode periods  $P_{n,1} = \nu_{n,1}^{-1}$  of high order gravity modes have an almost constant spacing,  $\Pi_1$ , the sampling theorem tells us that the frequency  $\mathcal{K}$  cannot be distinguished from its mirror image with respect to the Nyquist frequency,  $(2\Pi_1)^{-1}$ . This implies that the expression is invariant under the transformation,

$$(\mathcal{K}, \psi) \rightarrow \left( \Pi_1^{-1} - \mathcal{K}, \psi + \frac{1}{2} - \psi \right), \quad (19)$$

if the mode periods follow

$$P_{n,1} = (n + \varepsilon) \Pi_1, \quad (20)$$

in which  $\varepsilon$  is a constant that corresponds to the total phase offset introduced at the inner and outer turning points of the gravity-mode cavity. We do not need to consider the other Nyquist aliases because  $0 < \mathcal{K} < \Pi_1^{-1}$ , which will become clear later from equation (21). This type of degeneracy is identical to the core/envelope mirror symmetry discussed by Montgomery et al. (2003) (see Section 2.4.5). Strictly speaking, this degeneracy is approximate because the period spacing is not exactly constant in reality. It is still possible that the two sets of parameters  $(\mathcal{K}, \psi)$ , which are approximately related to each other by equation (19), give equally good fits to the data.

**Table 3.** The best fit values of the five parameters in equations (6) and (17) to explain the observed asymmetry in the frequency splittings  $\alpha_n$  in Fig. 1 after subtracting the contribution of rotation that is estimated based on our best evolutionary model A in Table 2. Two cases, 1 and 2, are considered because of the degeneracy about the glitch signature described by equation (19). In each case, the chi-squared per degrees of freedom ( $\chi^2/\text{df}$ ) is given in the last row.

	case 1	case 2
parameters of the magnetic effect		
$a$ ( $10^{-4} \text{ d}^{-4}$ )	$-1.18 \pm 0.08$	$-1.13 \pm 0.07$
$b$ ( $10^{-5} \text{ d}^{-2}$ )	$4.3 \pm 0.6$	$4.0 \pm 0.6$
parameters of the glitch effect		
$\mathcal{A}$ ( $10^{-5} \text{ d}$ )	$-1.6 \pm 0.1$	$-1.51 \pm 0.09$
$\mathcal{K}$ ( $\text{d}^{-1}$ )	$7.7 \pm 0.1$	$29.9 \pm 0.1$
$\psi$	$0.14 \pm 0.09$	$0.57 \pm 0.09$
$\chi^2/\text{df}$	0.997	0.732

#### 2.4.4 Combined effects of the magnetic field and the glitch

We fit in total five parameters, two ( $a$  and  $b$ ) in equation (6) and three ( $\mathcal{A}$ ,  $\mathcal{K}$  and  $\psi$ ) in equation (17), to the difference  $\alpha_n - \alpha_n^{(\text{rot})}$ . We exclude from the fitting the two data points at  $\nu_{n,1,0} = 1.13 \text{ d}^{-1}$  and  $1.20 \text{ d}^{-1}$ . The former clearly follows a different trend from the others, while the latter cannot be explained by the assumed form of the glitch signature in equation (17). In fact, inclusion of these points makes the fitting much worse. Possible origins for the two points are discussed in Section 3.1. We use the `curve_fit` function in the SciPy library of Python to fit the remaining fifteen data points. We adopt as a set of initial guesses of the five parameters the values obtained during the preliminary steps to determine the type of the glitch in Section 2.4.3. We make another set of initial guesses using equation (19). The results originating from the first and second sets are referred to as cases 1 and 2, respectively.

The results of the fitting are presented in Table 3 for model A (see Table 2). We find that the fitting is good in both cases 1 and 2 since  $\chi^2/\text{df}$  is close to one, although the value in case 2 is slightly smaller. The fitted values of  $\alpha_n$  and the residuals are shown in Fig. 5.

Since  $\alpha_n^{(\text{rot})}$  weakly depends on the evolutionary models, we repeat the fitting for the two other evolutionary models (models B and C in Table 2) and find little difference in all of the five parameters.

We can make a simple remark about the configuration of the inferred magnetic field. The negative sign of  $a$  in Table 3 implies that  $|B_r|$  is larger on average near the equatorial region than in the polar region because of equation (15). Similarly, the positive sign of  $b$  means that  $|B_\phi|$  is more confined to the equator than the poles (see equation (16)).

#### 2.4.5 Properties of the glitch

Here we interpret the three parameters,  $\mathcal{A}$ ,  $\mathcal{K}$  and  $\psi$ , about the glitch. The fitted value of  $\mathcal{K}$  in Table 3 can be used to estimate the position of the glitch ( $r_*$ ) based on the relation,

$$\int_{r_{\text{in}}}^{r_*} \frac{N}{r} dr = \sqrt{2} \pi^2 \mathcal{K}, \quad (21)$$

which can be obtained by comparing equation (17) with equation (B22). Here,  $r_{\text{in}}$  means the inner edge of the gravity-mode cavity, which almost coincides with the outer boundary of the convective

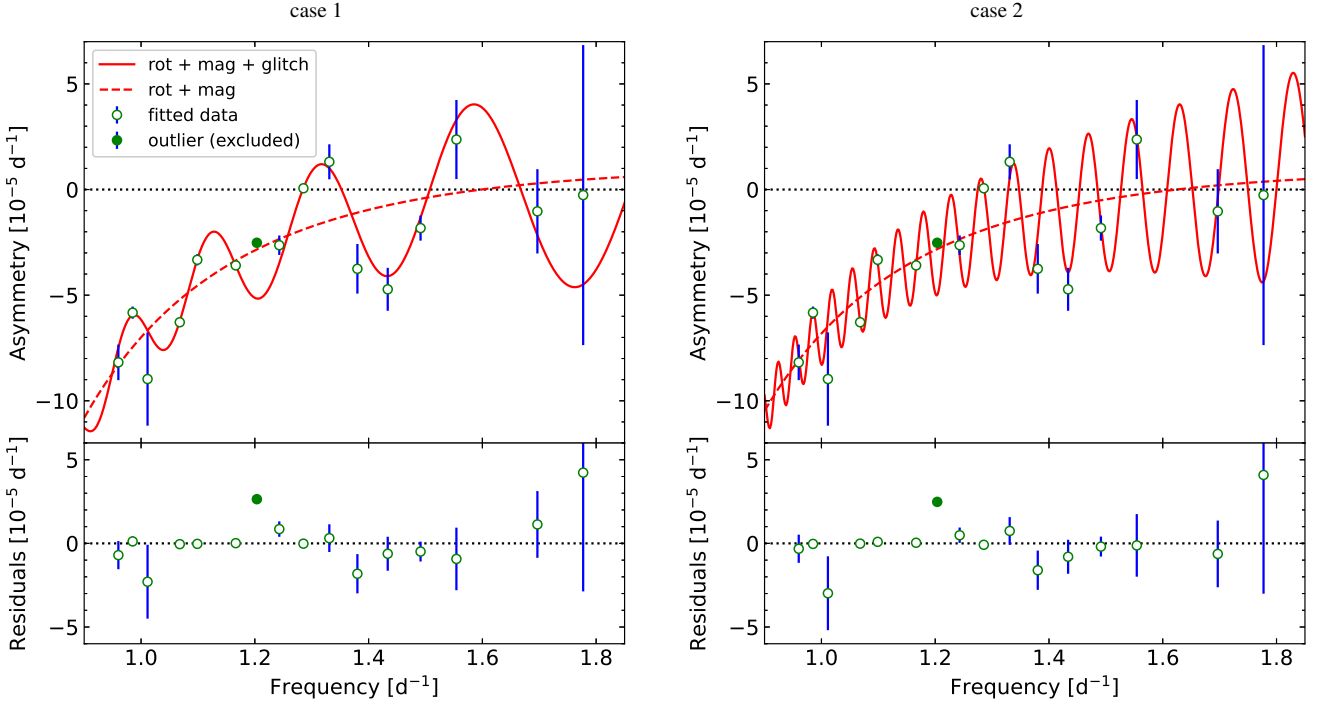


**Figure 5.** Asymmetry of frequency splittings  $a_n$  of KIC 9244992 fitted with the model that takes account of rotation, a magnetic field and a glitch (upper part of each panel) and the residuals (lower part). The results for the two cases, 1 and 2 (see Table 3), with different positions of the glitch (see Fig. 6), are presented in the left and right panels, respectively. The rotation effect is estimated based on our best evolutionary model (model A in Table 2). In each panel, there are two data points excluded from the fitting, one at  $1.20 \text{ d}^{-1}$  indicated by the filled circle and the other at  $1.13 \text{ d}^{-1}$ , whose ordinate is outside the plot range (Fig. 1). See Section 3.1 for the possible origins of these points.

core. We use model A in Table 2 to obtain

$$\frac{r_*}{R} = \begin{cases} 0.0636 \pm 0.0002 & \text{in case 1,} \\ 0.298 \pm 0.003 & \text{in case 2.} \end{cases} \quad (22)$$

The two possible positions are shown in Fig. 6, together with the Brunt–Väisälä frequency and the hydrogen mass fraction. The position in case 1 means that the discontinuity is located in the layer of the steep gradient of the hydrogen profile, which is created when the convective core shrinks in mass during evolution of the star. It is plausible that some mixing processes near the boundary between the convective core and the radiative envelope could generate the discontinuity in the first derivative of the hydrogen profile. On the other hand, the position in case 2 implies that the glitch is located deep in the radiative region, where it is not clear how to make a discontinuous structure in general. Because of this, case 1 is preferable to case 2 from a physical point of view.

The amplitude of the glitch signature  $\mathcal{A}$  is related to that of the step function  $\mathfrak{D}_1^{(1)}$  that describes the discontinuity in the quadrupole component of the Brunt–Väisälä frequency (see equation (B21)). The relation is given by

$$\mathfrak{D}_1^{(1)} = -\frac{8\sqrt{5}\pi^3}{3} \frac{\mathcal{A}}{\Pi_1}, \quad (23)$$

in which  $\Pi_1$  is the period spacing defined by equation (B14). Using the fitted value in Table 3 and the structure of model A in Table 2, we obtain

$$\mathfrak{D}_1^{(1)} = \begin{cases} 0.020 \pm 0.001 & \text{in case 1,} \\ 0.018 \pm 0.001 & \text{in case 2.} \end{cases} \quad (24)$$

The constant factor in equation (23) is equal to 33.2, which implies

that the size of the glitch signature  $\mathcal{A}$  is sensitive only weakly to the amplitude of the discontinuity. The positive sign of  $\mathfrak{D}_1^{(1)}$  means that the quadrupole component of the Brunt–Väisälä frequency decreases in the radial direction at the glitch, which in turn implies that (the quadrupole component of) the density gradient becomes less steep. If the Brunt–Väisälä frequency is dominated by the composition gradient, the gradient of the mean molecular weight also becomes less steep across the discontinuity. However, there is a warning at this point. The sign of  $\mathfrak{D}_1^{(1)}$  could be opposite because of the degeneracy given by equation (18).

We now turn to  $\psi$ , which is related to the phase lag ( $\varphi_{\text{in}}$ ) at the inner turning point of the gravity-mode cavity (see equation (A58)), by  $\psi = \varphi_{\text{in}}/\pi$ . We can compare  $\psi$  in Table 3 with its theoretical value of 0.25, which corresponds to  $\varphi_{\text{in}} = \pi/4$  (Unno et al. 1989) to conclude that they are consistent with each other in case 1 because the difference is only 1.2 times greater than the uncertainty. The corresponding factor in case 2 increases to at most 1.9 if we accept the change,

$$(\mathcal{A}, \psi) = (-1.51, 0.57) \rightarrow (1.51, 0.07), \quad (25)$$

based on equation (18).

## 2.5 Strengths of the magnetic field

We can infer the properties of the internal magnetic field based on equations (7) and (8). However, these expressions are in the asymptotic limit, which is less accurate in the outer layers of the star. We carefully examine this problem and establish more robust estimates of the field strengths.

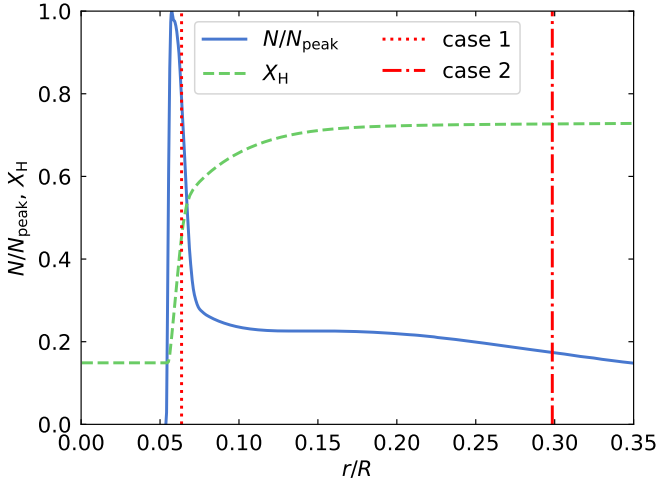


**Figure 6.** Two possible positions of the aspherical buoyancy glitch in fractional radius ( $r/R$ ) indicated by the vertical dotted and dashed lines. The solid curve represents the Brunt–Väisälä frequency ( $N$ ) normalised by the peak value ( $N_{\text{peak}}$ ) at  $r/R = 0.06$ , while the dashed curve stands for the hydrogen mass fraction ( $X_H$ ). This plot is based on the structure of model A in Table 2.

### 2.5.1 Asymptotic expressions for the lower bounds to the strengths of the field

We first illustrate the principle of estimating the lower bounds of the strengths of the field. The parameter  $a$  can be interpreted by equation (7). Using  $S_r$  of the evolutionary models, we can estimate  $\langle W_r B_r^2 \rangle$ , which in turn can be used to constrain the lower bound to the root-mean-square of the radial component of the magnetic field  $B_r^{\text{min}}$ . For negative values of  $\langle W_r B_r^2 \rangle$ , we can utilise the relation

$$\langle B_r^2 \rangle > -2\langle W_r B_r^2 \rangle = \frac{2(-a)}{S_r} \quad (26)$$

(see Li et al. 2022). Similarly, in equation (8) we may use  $b$  in Table 3 and  $S_h$  of the models to estimate  $\langle W_\phi B_\phi^2 \rangle$ , which imposes a constraint on the lower bound to the root-mean-square of the azimuthal component,  $B_\phi^{\text{min}}$ , by the relation,

$$\langle B_\phi^2 \rangle > -4\langle W_\phi B_\phi^2 \rangle = \frac{4b}{(-S_h)}. \quad (27)$$

In order to use equations (26) and (27), we need to assume the radius  $r_{\text{up}}$ , outside which no magnetic field exists at all. However, there is no direct observational constraint on  $r_{\text{up}}$ . Instead, we may set  $r_{\text{up}}$  to the outer edge of the gravity-mode cavity, but this approach also has a problem because equations (26) and (27) are valid only in the asymptotic limit, which is not realised very well in the outer layers. Therefore, we consider it improper to apply equations (26) and (27) as they are. In the following sections, we carefully examine the problems of these relations to revise them.

### 2.5.2 Problem of the asymptotic expressions

An essential point of the arguments in Section 2.5.1 is that  $a$  and  $b$  are independent of the mode frequencies. This is correct only in the asymptotic limit, while their general expressions are given by

$$a_n \equiv \frac{3}{128\pi^5} \int_0^R \hat{\mathcal{K}}_r^{(n,1)} \overline{W_r B_r^2} dr \quad (28)$$

and

$$b_n \equiv -\frac{9}{32\pi^3} \int_0^R \hat{\mathcal{K}}_\phi^{(n,1)} \overline{W_\phi B_\phi^2} dr, \quad (29)$$

in which  $\hat{\mathcal{K}}_r^{(n,1)}$  and  $\hat{\mathcal{K}}_\phi^{(n,1)}$  are defined by

$$\hat{\mathcal{K}}_r^{(n,1)} \equiv \frac{(2\pi\nu_{n,1})^2 r^2 \left(\frac{d\xi_{h,n,1}}{dr}\right)^2}{\int_0^R (\xi_{r,n,1}^2 + 2\xi_{h,n,1}^2) \rho r^2 dr} \quad (30)$$

and

$$\hat{\mathcal{K}}_\phi^{(n,1)} \equiv \frac{2\xi_{h,n,1}^2}{\int_0^R (\xi_{r,n,1}^2 + 2\xi_{h,n,1}^2) \rho r^2 dr}, \quad (31)$$

respectively (see Appendix A6). Here,  $\xi_{r,n,\ell}$  and  $\xi_{h,n,\ell}$  represent the radial and horizontal displacements, respectively, with radial order  $n$  and spherical degree  $\ell$ . The asymptotic expressions for  $\hat{\mathcal{K}}_r^{(n,1)}$  and  $\hat{\mathcal{K}}_\phi^{(n,1)}$  are provided by

$$\hat{\mathcal{K}}_r^{\text{asympt}} \equiv \frac{\frac{N^3}{\rho r^3}}{\int_G \frac{N}{r} dr} \quad (32)$$

and

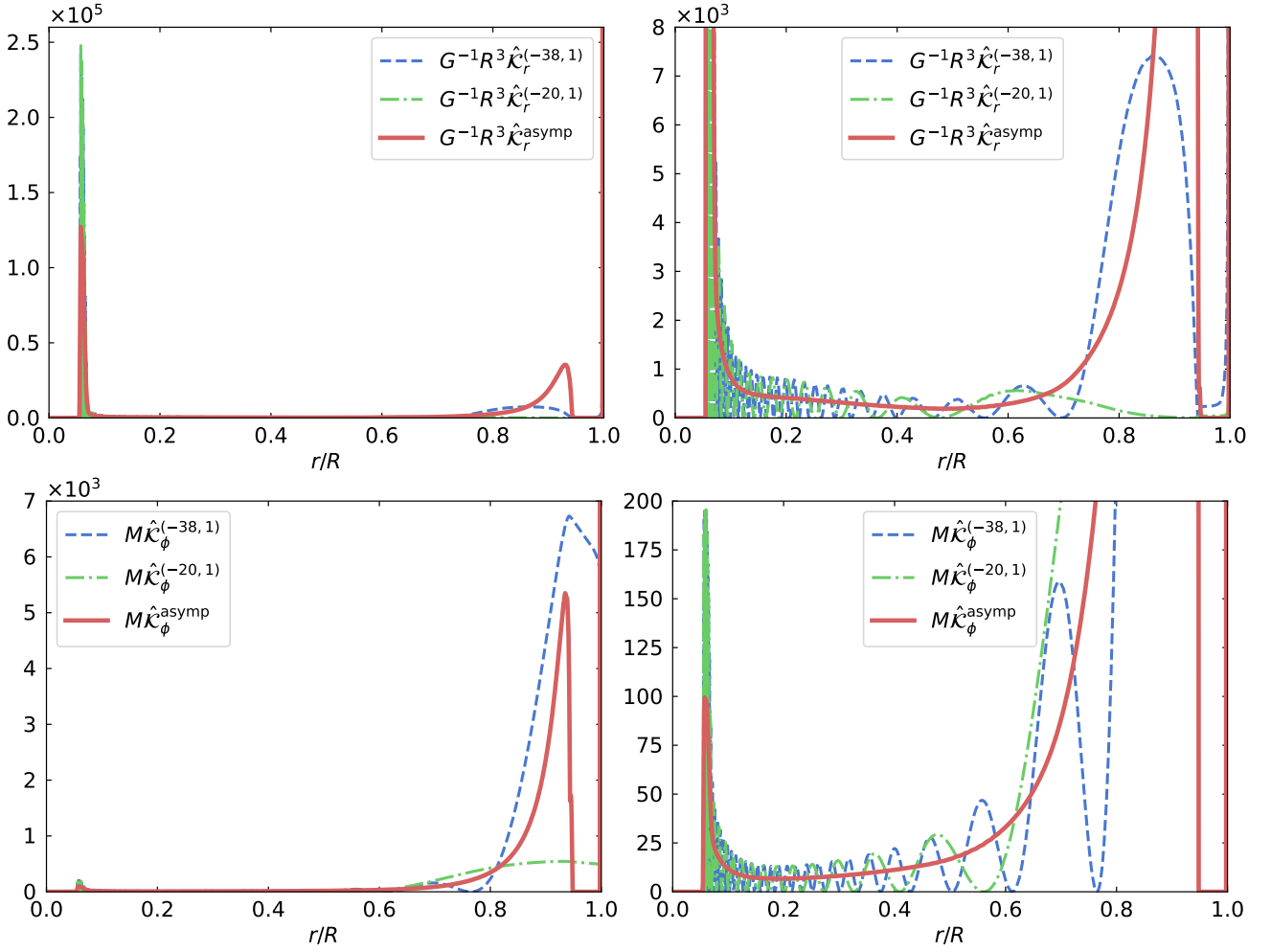
$$\hat{\mathcal{K}}_\phi^{\text{asympt}} \equiv \frac{\frac{N}{\rho r^3}}{\int_G \frac{N}{r} dr}. \quad (33)$$

Fig. 7 shows the profiles of  $\hat{\mathcal{K}}_r^{(n,1)}$  (with  $n = -38, -20$ <sup>1</sup>) and  $\hat{\mathcal{K}}_r^{\text{asympt}}$  in the upper panels and  $\hat{\mathcal{K}}_\phi^{(n,1)}$  (with  $n = -38, -20$ ) and  $\hat{\mathcal{K}}_\phi^{\text{asympt}}$  in the lower panels for model A in Table 2. We observe in the upper panels that the profiles of  $\hat{\mathcal{K}}_r^{(n,1)}$  are highly concentrated around  $r/R \approx 0.06$  and so oscillatory in the inner layers ( $r/R \lesssim 0.5$ ) that their average behaviour can be described by  $\hat{\mathcal{K}}_r^{\text{asympt}}$  very well. The high peak is located in the layers of the steep gradient of chemical compositions just outside the convective core. The oscillatory behaviour occurs because the radial wave number  $k_r$  is large enough. On the other hand, in the outer layers ( $r/R \gtrsim 0.5$ ), we find that (1) the profiles of  $\hat{\mathcal{K}}_r^{(n,1)}$  become rapidly less oscillatory, that (2) the amplitude of  $\hat{\mathcal{K}}_r^{\text{asympt}}$  increases steeply and that (3) the amplitude of  $\hat{\mathcal{K}}_r^{(n,1)}$  differs significantly between the two modes. The reason for point (1) is that  $k_r$  becomes smaller due to the decrease in the Lamb frequency rather than the Brunt–Väisälä frequency (see Fig. 12 of S15). In fact, unlike the higher-order mode (with  $n = -38$ ), the outer turning point of the lower-order mode (with  $n = -20$ ) is not fixed by the Brunt–Väisälä frequency but the Lamb frequency, which explains point (3). Point (2) is due to the lower density in the near-surface layers. All of the three points demonstrate that the asymptotic expression  $\hat{\mathcal{K}}_r^{\text{asympt}}$  becomes inaccurate in the outer layers.

In the lower panels of Fig. 7,  $\hat{\mathcal{K}}_\phi^{(n,1)}$  and  $\hat{\mathcal{K}}_\phi^{\text{asympt}}$  show similar structures to  $\hat{\mathcal{K}}_r^{(n,1)}$  and  $\hat{\mathcal{K}}_r^{\text{asympt}}$ , respectively, although the peak of  $\hat{\mathcal{K}}_\phi^{\text{asympt}}$  in the innermost radiative region is much smaller than that in the outermost radiative region around  $r/R \approx 0.93$ . The much higher weight in the outer layers is because  $\hat{\mathcal{K}}_\phi^{\text{asympt}}$  is proportional to a lower power of  $N$  than  $\hat{\mathcal{K}}_r^{\text{asympt}}$ . The largest amplitude of  $\hat{\mathcal{K}}_\phi^{(n,1)}$  in the outer layers appears to imply that these layers contribute significantly to the integral in equation (29). However, we argue in the next section that this is not true.

<sup>1</sup> We follow Takata (2006) for the definition of the radial order  $n$ .





**Figure 7.** Profiles of  $\hat{\mathcal{K}}_r^{(n,1)}$  (with  $n = -38, -20$ ) and  $\hat{\mathcal{K}}_r^{\text{asymp}}$  normalised by  $GR^{-3}$  (upper panels) and  $\hat{\mathcal{K}}_\phi^{(n,1)}$  (with  $n = -38, -20$ ) and  $\hat{\mathcal{K}}_\phi^{\text{asymp}}$  normalised by  $M$  (lower panels) as functions of the fractional radius  $r/R$  for model A in Table 2. The frequencies of the modes with  $n = -38$  and  $n = -20$  are  $0.96 \text{ d}^{-1}$  and  $1.79 \text{ d}^{-1}$ , respectively. The left panels are the plots to see the overall structure, while the right panels have smaller ordinate scales to resolve the oscillatory behaviour of  $\hat{\mathcal{K}}_r^{(n,1)}$  and  $\hat{\mathcal{K}}_\phi^{(n,1)}$ .

### 2.5.3 Maximum field strengths of the analysis at each radius

Here, we recall the two assumptions given in Section 2.3. The first one is that the first-order rotation effect is much larger than the direct effect of the magnetic field. The former and latter can be estimated by the dimensionless parameters,

$$s \equiv \frac{2v_{\text{rot}}}{v}, \quad (34)$$

and

$$s_m \equiv \left( \frac{B_r}{B_r^{\text{UL}}} \right)^2, \quad (35)$$

respectively, in which  $B_r^{\text{UL}}$  is defined by equation (A71). Here,  $s$  is called the spin parameter and provides the ratio of the Coriolis force and the inertial term, whereas  $s_m$  is the ratio of the horizontal component of the Lorentz force and that of the pressure gradient. The condition of  $s_m \ll s$  (for  $\ell = 1$ ) yields

$$|B_r| \ll B_r^{\text{max}} \equiv \sqrt{64\pi^5 v_{\text{rot}} v^3 \rho} \frac{r}{N}. \quad (36)$$

The second assumption is that the magnetic deformation of the equilibrium structure is smaller than the rotational deformation. The

effect of the magnetic deformation can be estimated by the ratio between the magnetic and gas pressure ( $p$ ),

$$\tau_{\text{mag}} \equiv \frac{B^2}{8\pi p}, \quad (37)$$

whereas that of the rotational deformation can be estimated by the ratio between the centrifugal force at the equator and the gravity,

$$\tau_{\text{rot}} \equiv \frac{r(2\pi v_{\text{rot}})^2}{g}, \quad (38)$$

where  $g$  is the gravitational acceleration. Then, the condition of  $\tau_{\text{mag}} \ll \tau_{\text{rot}}$  means

$$B \ll B^{\text{max}} \equiv \sqrt{\frac{32\pi^3 v_{\text{rot}}^2 r p}{g}}. \quad (39)$$

The profiles of  $B^{\text{max}}$  and  $B_r^{\text{max}}$  are shown in Fig. 8. We observe that  $B^{\text{max}}$  decreases monotonically and rapidly because  $p$  does so towards the surface. Although the amplitude of  $\hat{\mathcal{K}}_\phi^{(n,1)}$  roughly increases in proportion to the inverse of  $\rho$  in the outer layers of the star,  $\hat{\mathcal{K}}_\phi^{(n,1)}(B^{\text{max}})^2$  becomes smaller for larger radii because  $p/\rho$

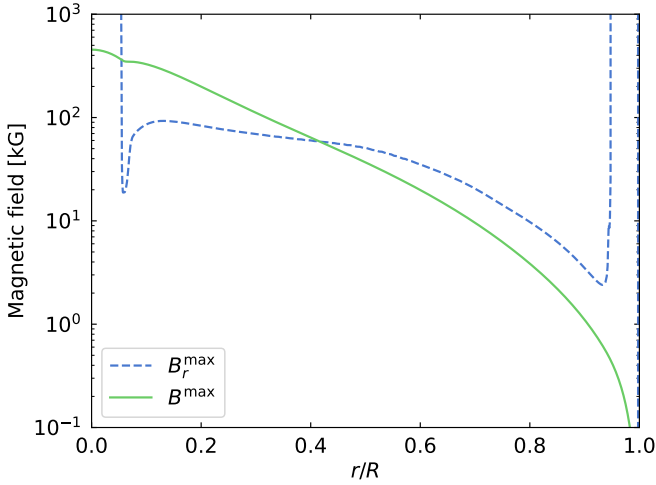


**Figure 8.** The maximum strengths of the radial component of the magnetic field ( $B_r^{\max}$ ) and the total magnetic field ( $B^{\max}$ ) that come from the assumptions of the present analysis. The condition of  $|B_r| < B_r^{\max}$  means that the Coriolis force contributes to the restoring force of the oscillation more importantly than the Lorentz force, while  $|B| < B^{\max}$  means that the equilibrium structure is deformed by the centrifugal force more significantly than the Lorentz force. Model A in Table 2 is used. The rotation period and the oscillation frequency are assumed to be 64 d and  $1 \text{ d}^{-1}$ , respectively.

decreases. We therefore understand that the contribution of the outer layers to the integral in equation (29) is small.

We may stress the meanings of these maximum strengths. The estimates for the radial and total magnetic fields at each radius must not be larger than  $B_r^{\max}$  and  $B^{\max}$ , respectively, for the analysis to be self-consistent. If this is not the case, the fundamental relation of the present analysis, equation (3), cannot be justified. The fact that equation (3) provides good fits to the data suggests, but does not prove, that these conditions are actually satisfied. Since  $B^{\max} < B_r^{\max}$  for  $r/R > 0.42$ , we concentrate on  $B^{\max}$  to discuss the contribution from the near-surface layers to the integrals in equation (29).

#### 2.5.4 Estimates for the root-mean-square of the strengths of the field

We modify equations (26) and (27), taking into account the two problems, the poor asymptotic expressions in the outer layers and the maximum strengths of the field in the analysis. Since the problems are more severe for  $B_\phi$  than  $B_r$ , we first discuss  $B_\phi$ .

Since  $W_\phi \geq -1/4$  (see equation (16)), we find from equation (29)

$$\frac{128\pi^3}{9} b_n \leq \int_0^R \hat{\mathcal{K}}_\phi^{(n,1)} \overline{B_\phi^2} dr = I_{n,\text{in}} + I_{n,\text{out}}, \quad (40)$$

where we have separated the integral in two parts at radius  $r_{\text{up}}$  by introducing

$$I_{n,\text{in}} \equiv \int_0^{r_{\text{up}}} \hat{\mathcal{K}}_\phi^{(n,1)} \overline{B_\phi^2} dr \quad (41)$$

and

$$I_{n,\text{out}} \equiv \int_{r_{\text{up}}}^R \hat{\mathcal{K}}_\phi^{(n,1)} \overline{B_\phi^2} dr. \quad (42)$$

The idea is to choose  $r_{\text{up}}$  such that the asymptotic expression  $\hat{\mathcal{K}}_\phi^{\text{asympt}}$  is accurate enough for  $r \leq r_{\text{up}}$  while keeping  $I_{n,\text{out}}$  small enough.

We may substitute  $\hat{\mathcal{K}}_\phi^{\text{asympt}}$  into  $\hat{\mathcal{K}}_\phi^{(n,1)}$  in  $I_{n,\text{in}}$ . The error of this

approximation can be estimated as

$$\frac{9}{128\pi^3 b_n} \left| I_{n,\text{in}} - \int_{r_{\text{in}}}^{r_{\text{up}}} \hat{\mathcal{K}}_\phi^{\text{asympt}} \overline{B_\phi^2} dr \right| \leq c_n, \quad (43)$$

in which we have defined

$$c_n \equiv \frac{9\nu_{n,1}}{128\sqrt{2}\pi^2 b} \left( \int_G \frac{N}{r} dr \right)^{-1} \left[ \frac{(B^{\max})^2}{\rho r^2} \right]_{r=r_{\text{up}}}. \quad (44)$$

Note that  $r_{\text{in}}$  in equation (43), which has been introduced in equation (21), means the inner edge of the gravity-mode cavity. In deriving equation (44), we have substituted equation (A58) into equation (41), and performed integration by parts.

On the other hand, we may constrain the upper limit of the relative contribution of  $I_{n,\text{out}}$  to be

$$\frac{9I_{n,\text{out}}}{128\pi^3 b} \leq d_n \equiv \frac{9}{128\pi^3 b} \int_{r_{\text{up}}}^R \hat{\mathcal{K}}_\phi^{(n,1)} (B^{\max})^2 dr. \quad (45)$$

The relative errors  $c_n$  and  $d_n$  can be evaluated using the structure and the eigenfunctions of the equilibrium models in Table 2 together with the fitted values of  $b$  given in Table 3. We confirm for all the modes in the analysis of all the models in Table 2 and for the both cases of the glitch positions (cases 1 and 2)

$$c_n < \bar{c} = 0.012 \quad (46)$$

and

$$d_n < \bar{d} = 0.1 \quad (47)$$

for

$$x_{\text{up}} = \frac{r_{\text{up}}}{R} = 0.5. \quad (48)$$

Although we may choose other values of  $x_{\text{up}}$ , we regard the value in equation (48) as fiducial. Note that this corresponds to the radial coordinate of  $r = 1.02 R_\odot$  and the mass coordinate of  $M_r = 1.42 M_\odot$  (98 per cent of the total mass) in model A.

Using equations (40), (43) and (45) with  $b_n = b$ , we can revise equation (27) as

$$\langle B_\phi^2 \rangle^{1/2} > B_\phi^{\min} \equiv \left[ \frac{4b}{(-S_h)} (1 - \bar{d}) \right]^{1/2}, \quad (49)$$

in which we have neglected  $\bar{c}$  because it is smaller than  $\bar{d}$  by an order-of-magnitude (see equations (46) and (47)). Here, the integral domain  $G_B$  that appears in the definition of  $S_h$  (see equation (10)) is between  $r = r_{\text{in}}$  and  $r = r_{\text{up}}$ .

In order to obtain the corresponding expression for  $B_r$ , for simplicity we make an additional assumption,

$$\left| \frac{\int_{r_{\text{up}}}^R \hat{\mathcal{K}}_\phi^{(n,1)} \overline{W_r B_r^2} dr}{\int_0^R \hat{\mathcal{K}}_\phi^{(n,1)} \overline{W_r B_r^2} dr} \right| \leq \frac{1}{4} \left| \frac{\int_{r_{\text{up}}}^R \hat{\mathcal{K}}_\phi^{(n,1)} \overline{W_\phi B_\phi^2} dr}{\int_0^R \hat{\mathcal{K}}_\phi^{(n,1)} \overline{W_\phi B_\phi^2} dr} \right|, \quad (50)$$

which roughly means that  $B_r$  is concentrated in the core region to the degree similar to or more than  $B_\phi$ . Then, also assuming that the error in the asymptotic expression is negligible for  $r \leq r_{\text{up}}$ , we can revise equation (26) as

$$\langle B_r^2 \rangle^{1/2} > B_r^{\min} \equiv \left[ \frac{2(-a)}{S_r} (1 - \bar{d}) \right]^{1/2}. \quad (51)$$

Table 4 provides  $B_r^{\min}$  and  $B_\phi^{\min}$  for the three evolutionary models in Table 2 (A, B and C) and the two positions of the aspherical glitch (cases 1 and 2) with  $x_{\text{up}} = 0.5$ . The results for model A and case 1,  $B_r^{\min} = 3.5 \pm 0.1 \text{ kG}$  and  $B_\phi^{\min} = 92 \pm 7 \text{ kG}$ , are completely consistent

**Table 4.** Estimates of the lower bounds to root-mean-squares of  $B_r$  and  $B_\phi$ . The assumed models are those in Table 2, while cases 1 and 2 are different from each other in the position of the glitch (see Fig. 6). The upper limit of the integrals in the numerators of equations (9) and (10) is set to  $x_{\text{up}} = 0.5$  in unit of the fractional radius.

Model	A*	B	C
$B_r^{\text{min}}$ (kG)			
case 1	$3.5 \pm 0.1$	$3.7 \pm 0.1$	$3.6 \pm 0.1$
case 2	$3.4 \pm 0.1$	$3.6 \pm 0.1$	$3.5 \pm 0.1$
$B_\phi^{\text{min}}$ (kG)			
case 1	$92 \pm 7$	$92 \pm 7$	$93 \pm 7$
case 2	$88 \pm 7$	$89 \pm 7$	$89 \pm 7$

Note. \* the best model (see S15).

with the other cases with different combinations of evolutionary models and glitch positions. The estimates for  $B_r^{\text{min}}$  and  $B_\phi^{\text{min}}$  are quite insensitive to the evolutionary models and the positions of the glitch. The fact that  $B_\phi^{\text{min}}$  is larger than  $B_r^{\text{max}}$  at  $r/R = 0.5$ , which is equal to 37 kG for model A (see Fig. 8), means that the field distribution within  $r/R \leq 0.5$  is biased to the core. We also confirm that  $B_r^{\text{min}}$  is well below  $B_r^{\text{max}}$  in Fig. 8. We finally note that if  $B_r = B_r^{\text{min}}$  and  $B_\phi = B_\phi^{\text{min}}$  for  $r/R \leq 0.5$ , the ratio of the magnetic pressure to the centrifugal force at the equator is equal to 0.04–0.7 outside the convective core for model A and case 1. This confirms one of the assumptions made in Section 2.3.

### 3 DISCUSSION

We have shown that the observed asymmetry of frequency splittings in KIC 9244992 can be explained by a model with an internal magnetic field, whose azimuthal component is much stronger than the radial component. Historically, it is well established that a small fraction (about ten per cent) of intermediate-mass main-sequence stars have strong and large-scale magnetic fields at the surface, which are associated with chemical peculiarities. Because of this, much attention has been paid to the surface of these stars. The result of this study enables us to move our focus to the interior of the stars with observational constraints. From the asteroseismic point of view, we have so far been able to constrain only the radial component of the internal magnetic field in red giants, which allows us to study only limited aspects of the magnetic problems in stars. On the other hand, the predominantly toroidal configuration in the main-sequence star revealed by the present study has opened the possibility of investigating the origin, the impact on the angular momentum transport, and the evolutionary change of the field from a new angle. Here, we discuss several topics concerning this result.

#### 3.1 Excluded data points

We exclude from the fitting two data points of the asymmetry of the frequency splittings, (1)  $a_n = 8.1 \times 10^{-5} \text{ d}^{-1}$  at  $\nu_{n,1} = 1.13 \text{ d}^{-1}$  (see Fig. 1) and (2)  $a_n = -2.5 \times 10^{-5} \text{ d}^{-1}$  at  $\nu_{n,1} = 1.20 \text{ d}^{-1}$  (see Fig. 5). We speculate on the origin of these points.

First, we point out a potential problem in the frequency analysis that the frequency determination of a mode can be perturbed by another mode with a very close frequency within the resolution and an amplitude above the noise level.

Actually, the problem of the close frequency influences not only the data analysis but also the physics of stellar oscillations. If there

are two modes with very close frequencies (close degeneracy), those frequencies could be perturbed as a result of mode interaction due to nonlinearity or rotation or magnetic fields. This might possibly cause a considerable effect in the frequency spectrum as a result of an avoided crossing.

In fact, checking the frequencies of model A, we find a quadrupolar mode with  $\nu_{-56,2} = 1.1347 \text{ d}^{-1}$ , which is close to the dipolar mode with  $\nu_{-32,1} = 1.1356 \text{ d}^{-1}$ , which corresponds to data point (1). Therefore, data point (1) could undergo a significant effect of close degeneracy. In addition, although the frequency difference between the two modes of  $9 \times 10^{-4} \text{ d}^{-1}$  is larger than the frequency resolution given by equation (2), it is possible that a small error in the evolutionary model shifts the theoretical frequencies to agree with each other within the resolution. Only one other mode has a closer  $\ell = 2$  mode frequency, which is the one at  $1.7 \text{ d}^{-1}$ . However, this mode has a much larger measurement uncertainty, so the influence of any mode interaction is difficult to discern. On the other hand, in the case of data point (2), there do not exist for  $2 \leq \ell \leq 4$  modes with such close frequencies to the dipolar one with  $\nu_{-30,1} = 1.2088 \text{ d}^{-1}$ . Still, there is an  $\ell = 5$  mode with  $\nu_{-118,5} = 1.2066 \text{ d}^{-1}$ , which differs by  $2 \times 10^{-3} \text{ d}^{-1}$  from the dipolar mode. This is itself not surprising because the period spacing becomes smaller (the spectrum becomes denser) for larger  $\ell$ , which implies a higher chance of finding a close frequency. Since we do not expect strong interaction between the  $\ell = 1$  and  $\ell = 5$  modes, the effect of the close degeneracy for data point (2) would be much smaller than for data point (1). Although this is qualitatively consistent with the fact that data point (2) is much closer to the best-fit curves than data point (1), we postpone detailed quantitative analysis to future work.

#### 3.2 Origin of the detected magnetic field

We may consider at least four possible origins of the detected magnetic field: (1) an interstellar field that is locked into the star (fossil field) (Section 3.2.1); (2) a field generated by the dynamo process in the convective core and moved or left in the radiative region (Section 3.2.3); (3) a field generated and maintained by a dynamo process of Tayler–Spruit type in the radiative region (Section 3.2.4); (4) a field generated by the magneto-rotational instability (MRI) during a merger process (Section 3.2.5). We also discuss the stability of the field (Section 3.2.2).

##### 3.2.1 Fossil field

During formation of an intermediate-mass star, weak magnetic fields that are embedded in the interstellar medium can become concentrated in the star as the medium collapses into it. Unless the fields are completely destroyed during the pre-main-sequence wholly convective phase, they are eventually locked in the radiative region of the star. If these fields relax to a stable configuration, they can survive for the timescale of magnetic diffusion, which is on the order of  $10^{10} \text{ yr}$  (longer than the lifetime of the main-sequence stage for a star with a mass  $\gtrsim 1.5 M_\odot$ ). While the problem of stability is discussed separately in Section 3.2.2, there have been many theoretical studies of the equilibrium structure of magnetic fields and its stability in the stellar radiative interior (e.g. Prendergast 1956; Woltjer 1960; Braithwaite & Spruit 2004; Braithwaite & Nordlund 2006; Braithwaite 2008; Duez & Mathis 2010; Duez et al. 2010b). There have also been studies about the effect of internal fields on stellar structure and evolution (e.g. Mestel & Moss 1977; Duez et al. 2010a). It certainly will be interesting to compare the result of the present analysis with

these works in detail, which is postponed to future work. Instead, we concentrate on the following issue here.

If the field originates from the interstellar field, we may expect it to extend outside the surface. This is not likely because our model with no surface field can explain the observed data quite well. In addition, if there were a large-scale surface magnetic field, which is generally inclined to the rotation axis, the oblique pulsator model (Kurtz 1990) would predict that all acoustic modes should show a multiplet structure in the frequency spectrum, whose components are equally split by the rotation frequency. This phenomenon is not detected in KIC 9244992 (see Table 3 of S15). Furthermore, there has been no confirmed detection of any large-scale magnetic field at the surface of any  $\gamma$  Dor (or  $\delta$  Sct- $\gamma$  Dor hybrid) stars (e.g. Thomson-Paressant et al. 2023; Hubrig et al. 2023).

One possible solution to this problem could come from the hypothesis of Jermyn & Cantiello (2020), which was proposed to explain the observed bimodal distribution of the surface magnetic fields of early-type main-sequence stars (e.g. Aurière et al. 2007; Lignières et al. 2014). A large-scale surface magnetic field could be destroyed by convective motions near the surface unless it is sufficiently strong. Then, a dynamo process would work in the subsurface convective zone to generate a much weaker small-scale field. We may examine this idea using simplified expressions. A sufficient condition for a magnetic field to suppress convection is given by

$$\frac{B_r^2}{B_r^2 + 8\pi\Gamma_1 p} > \nabla - \nabla_{\text{ad}} \quad (52)$$

(Gough & Tayler 1966). Here,  $\Gamma_1$  is the first adiabatic index, while  $\nabla$  and  $\nabla_{\text{ad}}$  mean the temperature gradient,  $d \ln T / d \ln p$ , and its adiabatic value,  $(\partial \ln T / \partial \ln p)_S$ , respectively, where  $S$  represents entropy. If the radial component of the fossil field,  $B_r$ , is strong enough to satisfy equation (52) for  $\nabla = \nabla_{\text{rad}}$ , where  $\nabla_{\text{rad}}$  is the radiative temperature gradient, then the convection is suppressed and the field keeps its large-scale structure on the surface of the star. Otherwise, the convective motions significantly modify the field to generate small-scale structures, which would lead to unstable configurations, and hence decay of the field.

Our best model of KIC 9244992 (model A) with  $1.45 M_\odot$  has only one subsurface convective zone in the outermost five per cent in radius ( $5 \times 10^{-6}$  in fractional mass), where hydrogen (H I), He I and He II undergo ionisation. An essential point is that the opacity in this zone is dominated by that of the ionisation of hydrogen, which results in very large values of  $\nabla_{\text{rad}}$  with the maximum value of  $\approx 400$ . Since the left-hand side of equation (52) is always smaller than one, this condition can never be satisfied in most of the convective zone, which implies that the magnetic field would not suppress the subsurface convection. However, the convection associated with the ionisation of hydrogen is so efficient that the strength of the dynamo-generated small-scale field should range between 0.4 kG (near the top of the zone) and 1.3 kG (near the bottom), values that are obtained by assuming the equipartition of energy between the magnetic field and the convective motion. This means that the field strength at the photosphere is about a few hundred Gauss, which has not been detected in any  $\gamma$  Dor stars so far. In summary, if we adopt the picture of Jermyn & Cantiello (2020), the large-scale fossil field could indeed be erased by the subsurface convection, but it would be replaced with a small-scale dynamo-generated field with considerable strength, which does not have any observational support. We therefore need to revise the picture or switch to some other mechanism (see e.g. Braithwaite & Spruit 2017) to explain the detected internal field of KIC 9244992 as a fossil one. In particular, since the assumption of the equipartition of energy could be too crude in the above discussion,

it is highly desirable to perform more detailed analysis about the interaction between the fossil magnetic field and the near-surface convection, which is outside the scope of this paper. We should also note that the present argument does not contradict Jermyn & Cantiello (2020), who considered only main-sequence models above  $2 M_\odot$ . In such higher-mass structures, the main focus is on the subsurface convection zones associated with the ionisation of He II and iron-group elements, which are much less efficient than the one with the ionisation of hydrogen, and hence would generate a much weaker field by dynamo.

### 3.2.2 Stability of the field

Apart from its origin, it is an interesting and important question whether the predominantly toroidal configuration found in the present analysis is stable or not (e.g. Braithwaite & Spruit 2017). On the one hand, it is well known from a theoretical point of view that purely toroidal magnetic fields are unstable against the Tayler instability (Tayler 1973). In fact, we may estimate the minimum strength of the toroidal component that is required for the Tayler instability to operate by overcoming the magnetic diffusion as

$$B_{\phi, \text{min}}^{(\text{TI})} \equiv (4\pi r \rho N_{\text{eff}})^{1/2} (\eta \Omega)^{1/4}, \quad (53)$$

in which  $\eta$  and  $\Omega$  stand for the magnetic diffusivity and the angular rotation rate, respectively. Equation (53) can be obtained by replacing  $N$  by  $N_{\text{eff}}$  in equation (8) of Spruit (2002). Here,  $N_{\text{eff}}$  is the effective Brunt-Väisälä frequency defined by

$$N_{\text{eff}}^2 \equiv \frac{\eta}{\kappa} N_T^2 + N_\mu^2, \quad (54)$$

in which  $\kappa$  means the thermal diffusivity and  $N_T$  and  $N_\mu$  represent the thermal and compositional part of the Brunt-Väisälä frequency, respectively. This replacement approximately takes into account the fact that the stabilising effect of thermal stratification becomes weaker due to thermal diffusion on the small spatial scales on which the Tayler instability occurs (see Spruit 2002). The profile of  $B_{\phi, \text{min}}^{(\text{TI})}$  is plotted in Fig. 9. It takes a maximum of  $\sim 30$  kG around  $r/R \sim 0.06$ , which is below  $B_{\phi, \text{min}}^{\text{min}}$  given in Table 4. This means that the detected field would be unstable against the Tayler instability if we neglect the poloidal component. On the other hand, from an observational point of view, no detectable change in the oscillation frequencies is found in KIC 9244992 over the nearly four-year period of the *Kepler* observation, which is much longer than the Alfvén timescale (the characteristic scale of the system  $l_s$  divided by the Alfvén velocity) of  $\sim 200$  d for  $B = 100$  kG,  $\rho = 30 \text{ g cm}^{-3}$  and  $l_s = 0.1 \times 2\pi R$ .

These considerations lead to the following question: can a purely toroidal field be stabilised by a small contribution of the poloidal component? In fact, the theoretical study of Braithwaite (2009) gives an affirmative answer to this question because the poloidal component gives a restoring force through bending of the field line against the horizontal motion, which is the main component of the Tayler instability. That study provides the stability condition for axisymmetric magnetic fields as

$$a_* \frac{E}{U} < \frac{E_p}{E} \lesssim 0.8, \quad (55)$$

in which  $E$ ,  $U$  and  $E_p$  are the total magnetic energy, the gravitational energy and the energy of the poloidal component, respectively. The parameter  $a_*$  is on the order of 10 for main-sequence stars. Although the condition assumes a purely radiative structure with no convective zone, we nonetheless apply it to KIC 9244992, which has a small convective core (eight per cent in mass in model A), to check the

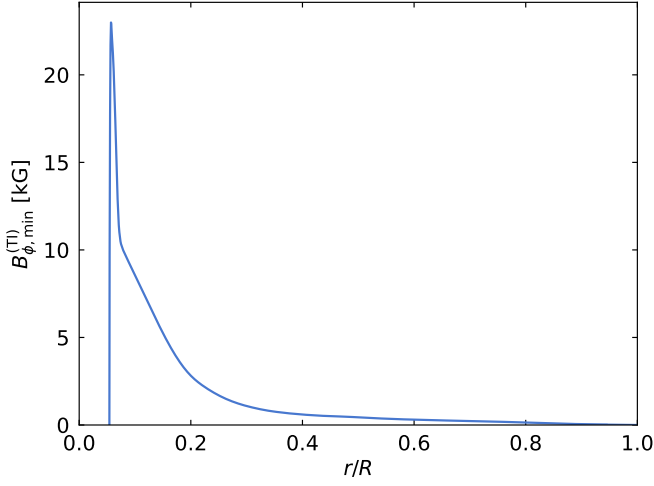


**Figure 9.** Profile of the minimum strength of the toroidal component of the magnetic field, which is defined by equation (53), for the Tayler instability to operate based on model A in Table 2 with the rotation period of 64 d.

field stability. Using the results in Table 4 and the structure of model A in Table 2, we obtain the following estimates:

$$\frac{E}{U} \sim 10^{-7} \quad (56)$$

and

$$\frac{E_p}{E} \sim 10^{-3}, \quad (57)$$

which clearly satisfy equation (55). This means that the detected field in KIC 9244992 is stable, if it is axisymmetric.

### 3.2.3 Convective dynamo

As for the second possibility, three-dimensional numerical simulations by Brun et al. (2005) and Hidalgo et al. (2024) have demonstrated that a dynamo can operate in the convective cores of A stars. Although these simulations assume a few (or more) times faster rotation rates than that of KIC 9244992, they show that the magnetic energy can reach at least the same order as the kinetic energy, implying an average field strength of several tens of kG in the convective core. This number is slightly smaller than, but is still on the same order as our inference of  $B_{\phi}^{\min} = 92 \pm 7$  kG in the inner radiative region. However, if we assume a crude estimate of

$$\left| \frac{B_{\phi}}{B_r} \right| \sim \frac{B_{\phi}^{\min}}{B_r^{\min}} \approx 30 \quad (58)$$

(see Table 4), this large value is not realised in the convective core in the cited simulations. The reason could possibly be given as follows.

If the field originates from the convective core, we need some mechanism to move it to the radiative region. Here, we may list two possibilities: direct transport by overshooting at the top of the convective core, or the shrinking of the convective core with stellar evolution leaving the generated magnetic field in the radiative region near the outer edge of the convective core. In either case, if there exists rotational shear (radial differential rotation) at the convective/radiative boundary, we may expect that the  $\Omega$  effect operates to convert the radial component into the toroidal component in the radiative region. Although S15 estimated that the degree of radial differential rotation of KIC 9244992 between the core and the envelope is only a few per

cent, this does not necessarily mean that the  $\Omega$  effect is negligible because it is cumulative after many rotations, and the degree of radial differential rotation could have been higher in the past.

Interestingly, the picture of the enhanced toroidal component due to rotational shear is supported by the recent numerical simulations of Ratnasingam et al. (2024) for a  $7-M_{\odot}$  main-sequence star with a rotation period of 4.04 d and a seed dipolar field of  $\sim 1$  G. These simulations with a higher mass and a shorter rotation period than KIC 9244992, which has the mass of  $\sim 1.5 M_{\odot}$  and a rotation period of 64 d, provide a ratio of the toroidal field energy to the poloidal field energy that is comparable to that implied by equation (58), although the asteroseismic analysis of KIC 9244992 rejects the presence of such strong rotational shear as found in the simulations in the near-core layers where the Brunt–Väisälä frequency has a sharp peak.

Because the steep gradient of chemical composition at the convective/radiative boundary is generated by the shrinking of the convective core along with evolution, the layers of the steep gradient are those once in the convective core, where the active dynamo process was in operation. In addition, since the steep gradient makes it difficult for the magnetic field to migrate to the outer region, it is possible that the field is totally confined in those layers. In this case, we may set  $x_{\text{up}} = 0.1$  and  $\delta = 0$  in equations (49) and (51) to obtain larger values of the lower bounds,

$$B_{\phi}^{\min} = 175 \pm 13 \text{ kG} \quad (59)$$

and

$$B_r^{\min} = 4.0 \pm 0.1 \text{ kG}, \quad (60)$$

respectively, for model A with the glitch position of case 1. These lead to an even larger ratio of

$$\left| \frac{B_{\phi}}{B_r} \right| \sim \frac{B_{\phi}^{\min}}{B_r^{\min}} \approx 40, \quad (61)$$

which means that the energy of the toroidal component is three orders of magnitude larger than that of the radial component. It is obvious that a more detailed comparison of the asteroseismic result with three-dimensional simulations with the appropriate parameters for KIC 9244992 is highly desirable.

### 3.2.4 Radiative dynamo

A promising mechanism for the dynamo process in the radiative region is the one proposed by Spruit (2002), which can be understood in the classical picture of the  $\alpha$ – $\Omega$  dynamo. Under radial differential rotation, the toroidal component of the magnetic field can be generated by stretching the (initially small) seed poloidal field (the  $\Omega$  effect). If the toroidal component becomes strong enough, the Tayler instability sets in, which essentially provides the  $\alpha$  effect to make the poloidal component from the toroidal component. Since the predominantly toroidal field is still unstable against the Tayler instability, the process continues. This mechanism (Tayler–Spruit dynamo) has received much attention, particularly because the magnetic field can transport angular momentum very efficiently in the radiative region of the stars (e.g. Cantiello et al. 2014; Moyano et al. 2023, 2024). However, the details of the mechanism are still under active debate, and more studies are clearly needed to understand its whole picture (e.g. Zahn et al. 2007; Fuller et al. 2019; Petridemange et al. 2023, 2024).

Having said all this, the first question to ask is whether the current structure of KIC 9244992 satisfies the condition for the Tayler–Spruit dynamo or not. In order to check this, we plot in Fig. 10 the minimum



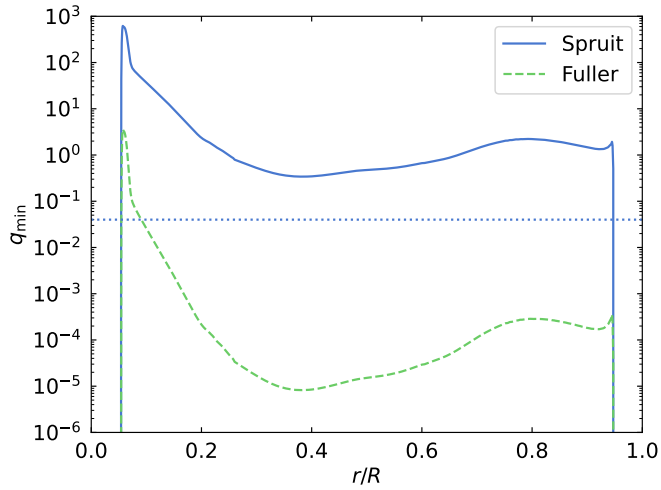


**Figure 10.** The minimum values of the gradient of the rotation rate,  $q$ , defined by equation (62), for the Taylor–Spruit dynamo to operate. The structure of model A in Table 2 is assumed with the rotation period of 64 d. Two cases are considered: One proposed by Spruit (2002) as in equation (63) (solid line) and the other by Fuller et al. (2019) as in equation (64) (dashed line). The horizontal dotted line indicates the asteroseismic estimate by S15 (equation (65)).

values of the degree of differential rotation,  $q$ , defined by

$$q \equiv \left| \frac{d \ln \Omega}{d \ln r} \right|, \quad (62)$$

which is required to sustain the mechanism. The original argument of Spruit (2002) provides

$$q_{\min}^{\text{Spruit}} = \left( \frac{N_{\text{eff}}}{\Omega} \right)^{7/4} \left( \frac{\eta}{r^2 N_{\text{eff}}} \right)^{1/4}, \quad (63)$$

whereas Fuller et al. (2019) reconsider the saturation mechanism based on turbulent dissipation of the perturbed field rather than the background toroidal field to present<sup>2</sup>

$$q_{\min}^{\text{Fuller}} = \left( \frac{N_{\text{eff}}}{\Omega} \right)^{5/2} \left( \frac{\eta}{r^2 \Omega} \right)^{3/4}. \quad (64)$$

On the other hand, S15 constrain the difference between the core and envelope rotation rates, which implies

$$q \approx 0.04. \quad (65)$$

We thus find  $q < q_{\min}^{\text{Spruit}}$  in the entire radiative region, which means that the Taylor–Spruit dynamo does not work in KIC 9244992 at least in its original form proposed by Spruit (2002). We also observe  $q < q_{\min}^{\text{Fuller}}$  near the peak around  $r/R = 0.06$ , which means that the Fuller-type mechanism can work only in the radiative region above the layer of the steep gradient of chemical compositions.

The next point to check is whether the field strengths detected are consistent with the prediction of the theory by Fuller et al. (2019). We therefore plot in Fig. 11 the radial and azimuthal components of the field based on equations (23) and (22) of Fuller et al. (2019), assuming equation (65) and the rotation period of 64 d. We confirm that the predicted azimuthal component has its maximum of 16 kG around  $r/R = 0.20$  for  $0.06 \leq r/R \leq 0.94$ , while the maximum of the radial component is found to be 0.014 kG around  $r/R = 0.34$  in

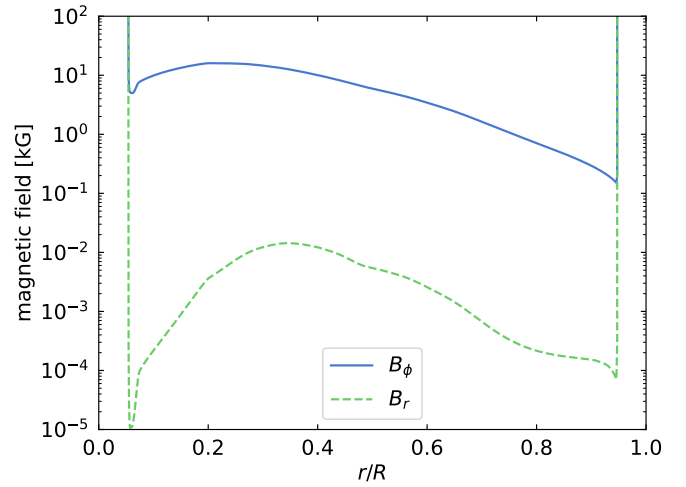


**Figure 11.** Profiles of the radial ( $B_r$ ) and azimuthal ( $B_\phi$ ) components of the magnetic field by the dynamo mechanism of Fuller et al. (2019). The structure of model A in Table 2 is assumed with the rotation period of 64 d and equation (65) for the gradient of the rotation rate.

the same range. For both components, the predicted values are well below the seismically estimated lower bound given in Table 4. We neglect the divergent trends of  $B_\phi$  and  $B_r$  near the inner and outer boundaries of the radiative region. This is justified by the fact that the trends come from the assumption of a finite differential rotation (equation (65)) even near the boundaries, which is unrealistic because the angular momentum transport is so efficient as  $N_{\text{eff}} \rightarrow 0$  that the differential rotation would disappear quickly. We therefore conclude that the Fuller-type mechanism is not operative in KIC 9244992, either.

One remaining possibility is that the star used to have strong differential rotation in the past, which was removed by efficient angular momentum transport by the magnetic field generated by the Taylor–Spruit dynamo. After the differential rotation subsided, the field suffered from the Tayler instability, which could substantially modify the configuration to settle in with the detected strengths of the field components. However, unless the structure of the star changes significantly, this scenario has difficulty explaining the implied significant increase of the total magnetic energy as a result of the Tayler instability. Such significant structural change cannot come from the central condensation that occurs with single-star evolution. Only significant mass transfer or a merger would suffice, and the former is essentially ruled out by the non-detection of a companion (or remnant) via pulsation timing (Murphy et al. 2018) and the absence of eclipses or ellipsoidal variation in the light curve (S15). The final conclusion of this section is that the dynamo mechanism in the radiative region is unlikely to be the origin of the detected field in KIC 9244992.

### 3.2.5 Stellar merger

One of the remarkable properties of KIC 9244992 is that its rotation period of  $\sim 64$  d is much longer than the typical period of 1 d of  $\gamma$  Dor stars. One possible explanation is that the star is a product of stellar merger. In fact, KIC 11145123, which is another slowly rotating  $\delta$  Sct– $\gamma$  Dor hybrid pulsator with a similar mass and a rotation period of  $\sim 100$  d, is suspected to be a blue straggler (Kurtz et al. 2014; Takada-Hidai et al. 2017; Hattai et al. 2021). One reason for this is that the best evolutionary model constructed by Kurtz et al. (2014)

<sup>2</sup> For simplicity, we set  $\alpha = 1$  in equation (36) of Fuller et al. (2019).

has an initial helium abundance of 0.36, which is unusually high for a single-star model. Although this is not the case for the models of KIC 9244992 (see Table 2), it would still be worth examining the merger or mass-transfer processes, which are possible mechanisms to form blue stragglers.

Schneider et al. (2019) have numerically simulated such a merger process to successfully explain the properties of the blue straggler  $\tau$  Sco, which has a rotation period of 41 d and a surface magnetic field of a few hundred gauss. They find that a strong internal magnetic field is generated by MRI during the merger, and that the merger product experiences significant spin-down during the subsequent (thermal relaxation) phase, before reaching the main-sequence position on the HR diagram. Although the mass of their target ( $\sim 15 M_{\odot}$ ) is much larger than KIC 9244992, we may consider the possibility that the same physical processes are at work in both systems. This hypothesis can simultaneously explain (qualitatively) the internal magnetic field and the slow (and uniform) rotation, but it also implies that the star should have a strong surface magnetic field, which is not supported by the present analysis (as we discuss in Section 3.2.1). In this context, we may note that no surface magnetic field has been detected in KIC 11145123 by high-resolution spectroscopy (Takada-Hidai et al. 2017), while Gizon et al. (2016) conjecture the presence of a surface field much weaker than the Sun at its activity maximum based on the asymmetry of the frequency splittings of acoustic modes. In order for the merger hypothesis to hold, we need to explain how to confine the magnetic field in the stellar interior (see Section 3.2.1).

### 3.3 Comparison with the case of red giants

The present result of asteroseismic detection of the internal magnetic field in KIC 9244992 follows those of red-giant stars (Li et al. 2022; Deheuvels et al. 2023; Hatt et al. 2024). We compare the two cases in this section.

Li et al. (2022) estimate that the detected  $\langle B_r^2 \rangle^{1/2}$  of 30 to 100 kG at the RGB stage should originate from that between 3 and 5 kG at the main-sequence stage, assuming magnetic flux conservation. The fact that this range is consistent with our estimate of  $B_r^{\min}$  in Table 4 supports the idea that the detected fields in KIC 9244992 and red giants have the same physical origin.

If we compare the analysis between the two cases, the main difference is that the present result can detect not only the radial component but also the azimuthal component of the field, whereas only the radial component is so far constrained in the red-giant case. This is mainly because the gravity radial orders of  $\sim 30$  of the detected modes in KIC 9244992 are lower than those of  $\gtrsim 100$  in stars at the red-giant branch (RGB) stage (except during the very early phase). While mode frequencies are generally more sensitive to the radial component than to the azimuthal component (Section 2.3.2), the corresponding longer radial wavelengths (measured relative to the size of the gravity-mode cavity) lessen this effect in KIC 9244992. As a result, the frequency perturbation due to the azimuthal component can be detected more easily in KIC 9244992.

On the other hand, in the red-giant cases, we can estimate the average field strength,  $\langle B_r^2 \rangle^{1/2}$ , although the analysis for KIC 9244992 can provide only the lower bound,  $B_r^{\min}$ . This is because the red-giant analysis relies on the asymptotic frequency formula to fit individual frequencies, while the current analysis concentrates on the asymmetry of the frequency splitting. In fact, a similar fitting of individual frequencies is not straightforward for KIC 9244992 because of the significant contribution of the glitch (see Section 3.5).

### 3.4 Implications on angular momentum transport

The field strengths detected in KIC 9244992, which are given in Table 4, imply that the torque via Maxwell stresses, which is proportional to  $B_r B_{\phi}$ , is larger by three orders of magnitude than predicted by the mechanism of Fuller et al. (2019). The number would be even larger for the original Tayler–Spruit dynamo by Spruit (2002). Therefore, the angular momentum transport in KIC 9244992 is much more efficient than described by the dynamo mechanisms associated with the Tayler instability in the radiative zone. We may quantify this point based on the time scale. Under the assumption that  $\Omega$  depends only on the radius (shellular rotation), the angular momentum transport in the radial direction due to the magnetic field can be formulated as a diffusion process (e.g. Maeder 2009). The corresponding diffusion coefficient (effective viscosity) is given by

$$D_{\text{mag}} \equiv \frac{|B_r B_{\phi}|}{4\pi\rho q\Omega}. \quad (66)$$

Then, the time scale of the angular momentum transport for a characteristic length scale  $l_s$  can be estimated as

$$\begin{aligned} \tau_{\text{mag}} &\equiv \frac{l_s^2}{D_{\text{mag}}} = \frac{8\pi^2 \rho q l_s^2}{P_{\text{rot}} |B_r B_{\phi}|} \\ &= 681 q \left( \frac{\rho}{10^2 \text{ g cm}^{-3}} \right) \left( \frac{P_{\text{rot}}}{64 \text{ d}} \right)^{-1} \left( \frac{l_s}{R_{\odot}} \right)^2 \left| \frac{B_r}{3.5 \text{ kG}} \right|^{-1} \left| \frac{B_{\phi}}{92 \text{ kG}} \right|^{-1} \text{ yr}, \end{aligned} \quad (67)$$

in which  $P_{\text{rot}} = 2\pi/\Omega$  means the rotation period (as in equation (5)) and  $\rho = 10^2 \text{ g cm}^{-3}$  is a good estimate of the density at the top of the convective core. The length scale of  $l_s \approx R_{\odot}$  corresponds to fifty per cent of the total radius of model A. It is clear that, for KIC 9244992,  $\tau_{\text{mag}}$  is much shorter than the evolutionary time scale of  $\sim 10^9$  yr. This means that uniform rotation ( $q = 0$ ) is established very quickly in the layers with the magnetic field.

We may use this argument to reject, in a different way from that in Section 3.2.1, the possibility that the magnetic field extends to the surface layers. In this case, we may set  $x_{\text{up}} = 0.95$  (the base of the near-surface convective zone) to obtain  $B_r^{\min} = 2 \text{ kG}$  and  $B_{\phi}^{\min} = 13 \text{ kG}$  (for model A). Even with these lower values of the field strengths,  $\tau_{\text{mag}}$  is still so short that the observed value of  $q = 0.04$  cannot be retained for the evolutionary time scale. More precisely, assuming the two-zone structure, S15 estimate that the rotation rate in the inner forty per cent in radius is four per cent higher than that in the outer sixty per cent. The lower rotation rate in the outer region should have a significant contribution by the non-magnetic layers, where there is no efficient transport of angular momentum.

Apart from the angular momentum transport inside the star, the slow rotation of KIC 9244992 (with the period of  $\sim 64$  d) needs to be explained separately because the total angular momentum of the star is much smaller than typical  $\gamma$  Dor stars, which have rotation periods of  $\sim 1$  d. Since we interpret that there is no large-scale magnetic field at the surface, there is no chance for magnetic braking to operate. Other possibilities include binary interaction and/or mass transfers, which are all speculative at this stage.

### 3.5 Spherical counterpart of the aspherical glitch

We may expect to identify the spherical counterpart of the aspherical glitch in the period versus period spacing diagram, which is reproduced in Fig. 12. From equation (B22), we can derive the expression

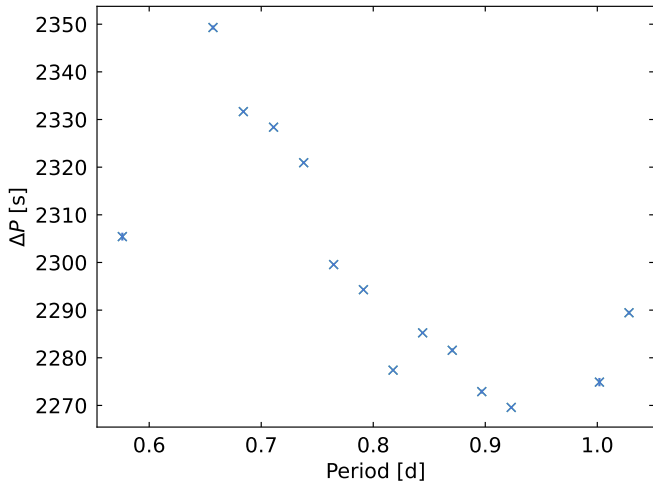


**Figure 12.** Diagram of period versus period spacing for high-order gravity modes of KIC 9244992.

for the period spacing as

$$P_{n+1} - P_n = \Pi_1 + \mathcal{A}^{(0)} \cos \left[ 2\pi \left( \mathcal{K} \frac{P_n + P_{n+1}}{2} - \psi \right) \right], \quad (68)$$

in which the amplitude of the oscillatory component is given by

$$\mathcal{A}^{(0)} \equiv -\frac{\Pi_1 \mathcal{D}_0^{(1)}}{4\sqrt{\pi^3}} \sin(\pi \mathcal{K} \Pi_1). \quad (69)$$

Assuming that the amplitude of the spherical component of the glitch is on the same order as the quadrupole component,  $|\mathcal{D}_0^{(1)}| \sim |\mathcal{D}_1^{(1)}|$ , we may use  $\mathcal{D}_1^{(1)}$  in equation (24),  $\Pi_1$  in Table 2 and  $\mathcal{K}$  in Table 3 to obtain

$$|\mathcal{A}^{(0)}| \sim 1 \text{ s}. \quad (70)$$

This estimate does not depend on the evolutionary model (models A or B or C) or the glitch position (cases 1 or 2).

However, our preliminary analysis finds it difficult to judge quantitatively whether the data contain the sinusoidal component given by the second term on the right-hand side of equation (68) with the expected amplitude given by equation (70) or not. This is because there are clearly multiple components with different amplitudes and periods. In fact, the dominant oscillatory component has a much larger amplitude of  $\sim 50$  s and a longer period of  $\sim 0.5$  d (see Fig. 12). This means that the nonlinearity (deviation from the sinusoidal function) of the dominant component is not negligible when we discuss a period difference on the order of seconds. Apart from the most dominant component, we may observe at most that the second most dominant component shows an oscillatory behaviour with an amplitude on the same order as that given by equation (70) and a period of  $\sim 0.1$  d, which is consistent with  $\mathcal{K}^{-1} = 0.13$  d for case 1 in Table 4. Since more careful treatment is necessary, we defer the detailed analysis to future work.

## 4 CONCLUSIONS

We have detected an internal magnetic field of KIC 9244992. The lower bound to the root-mean-squares of the radial and azimuthal components (with respect to the rotation axis) within 50 per cent in radius are estimated to be  $3.5 \pm 0.1$  kG and  $92 \pm 7$  kG, respectively. The

radial and azimuthal components are more confined to the equator than to the poles. The lower bound to the radial component is clearly incompatible with the prediction of the Taylor–Spruit dynamo, suggesting that the field could originate from other mechanisms, such as convective-core dynamos, fossil fields, and stellar mergers. We have also identified a signature of an aspherical discontinuous structure, which is located in the layers of steep chemical composition gradient just outside the convective core. We suppose that the structure is generated by some mixing processes at the boundary between the convective core and the radiative region. The discovery of the predominantly toroidal magnetic field has revealed a new aspect of magnetic fields in stars in general, generating many questions about their structure, origin and evolution.

## ACKNOWLEDGEMENTS

We thank NASA and the *Kepler* team for their revolutionary data. We also acknowledge the referee for constructive comments. MT thanks Ludovic Petitdemange, Facundo D. Moyano and Jim Fuller for their instructive and insightful comments about the present work. He is grateful to Rhita-Maria Ouazzani, Benoit Mosser and their colleagues at LIRA (formerly LESIA) of the Paris Observatory and Charly Pinçon at Université Paris-Saclay, Institut d’Astrophysique Spatiale for a lot of active scientific discussions under their warm hospitality and financial support based on the visiting fellow programme of the Paris Observatory in 2023 and 2025. This research was also supported by the Munich Institute for Astro-, Particle and BioPhysics (MIAPBP) which is funded by the Deutsche Forschungsgemeinschaft (DFG, German Research Foundation) under Germany’s Excellence Strategy – EXC-2094 – 390783311. MT was partially supported by JSPS KAKENHI Grant Numbers JP18K03695 and JP22K03672. SJM was supported by the Australian Research Council through Future Fellowship FT210100485.

## DATA AVAILABILITY

The data underlying this article will be shared on reasonable request to the corresponding author.

## REFERENCES

- Aerts C., Christensen-Dalsgaard J., Kurtz D. W., 2010, *Asteroseismology*. Springer, Dordrecht
- Antoci V., Cantiello M., Khalack V., Henriksen A., Saio H., White T. R., Buchhave L., 2025, *A&A*, **696**, A111
- Aurière M., et al., 2007, *A&A*, **475**, 1053
- Babcock H. W., 1947, *ApJ*, **105**, 105
- Bagnulo S., Landstreet J. D., 2021, *MNRAS*, **507**, 5902
- Benomar O., Takata M., Bazot M., Sekii T., Gizon L., Lu Y., 2023, *A&A*, **680**, A27
- Borra E. F., Landstreet J. D., Mestel L., 1982, *ARA&A*, **20**, 191
- Braithwaite J., 2008, *MNRAS*, **386**, 1947
- Braithwaite J., 2009, *MNRAS*, **397**, 763
- Braithwaite J., Nordlund Å., 2006, *A&A*, **450**, 1077
- Braithwaite J., Spruit H. C., 2004, *Nature*, **431**, 819
- Braithwaite J., Spruit H. C., 2017, *Royal Society Open Science*, **4**, 160271
- Brassard P., Wesemael F., Fontaine G., 1989, in Wegner G., ed., *White Dwarfs*. Springer Berlin Heidelberg, Berlin, Heidelberg, pp 258–262
- Briquet M., 2015, in *European Physical Journal Web of Conferences*. EDP, p. 05001 ([arXiv:1411.7549](https://arxiv.org/abs/1411.7549)), doi:10.1051/epjconf/201510105001
- Briquet M., Neiner C., Leroy B., Pápics P. I., MiMeS Collaboration 2013, *A&A*, **557**, L16

- Brown T. M., Latham D. W., Everett M. E., Esquerdo G. A., 2011, *AJ*, **142**, 112
- Brun A. S., Browning M. K., Toomre J., 2005, *ApJ*, **629**, 461
- Bugnet L., et al., 2021, *A&A*, **650**, A53
- Cantiello M., Mankovich C., Bildsten L., Christensen-Dalsgaard J., Paxton B., 2014, *ApJ*, **788**, 93
- Carrington R. C., 1863, Observations of the spots on the Sun: from November 9, 1853, to March 24, 1861, made at Redhill
- Coppée Q., Müller J., Bazot M., Hekker S., 2024, *A&A*, **690**, A324
- Cowling T. G., 1941, *MNRAS*, **101**, 367
- Dahlen F., Tromp J., 1998, Theoretical Global Seismology. Princeton University Press
- Das S. B., Chakraborty T., Hanasoge S. M., Tromp J., 2020, *ApJ*, **897**, 38
- Deheuvels S., Li G., Ballot J., Lignières F., 2023, *A&A*, **670**, L16
- Duez V., Mathis S., 2010, *A&A*, **517**, A58
- Duez V., Mathis S., Turck-Chièze S., 2010a, *MNRAS*, **402**, 271
- Duez V., Braithwaite J., Mathis S., 2010b, *ApJ*, **724**, L34
- Dziembowski W. A., Goode P. R., 1992, *ApJ*, **394**, 670
- Fuller J., Cantiello M., Stello D., García R. A., Bildsten L., 2015, *Science*, **350**, 423
- Fuller J., Piro A. L., Jermyn A. S., 2019, *MNRAS*, **485**, 3661
- García R. A., et al., 2014, *A&A*, **563**, A84
- Gel'fand I. M., Šapiro Z. Y., 1956, Amer. Math. Soc. Transl.(2), **2**, 207
- Gizon L., et al., 2016, Science Advances, p. in press
- Glampedakis K., Andersson N., 2007, *MNRAS*, **377**, 630
- Gough D. O., Tayler R. J., 1966, *MNRAS*, **133**, 85
- Gough D. O., Thompson M. J., 1990, *MNRAS*, **242**, 25
- Hale G. E., 1908, *ApJ*, **28**, 315
- Hale G. E., Ellerman F., Nicholson S. B., Joy A. H., 1919, *ApJ*, **49**, 153
- Hanasoge S. M., Woodard M., Antia H. M., Gizon L., Sreenivasan K. R., 2017, *MNRAS*, **470**, 1404
- Hathaway D. H., 2015, *Living Reviews in Solar Physics*, **12**, 4
- Hatt E. J., et al., 2024, *MNRAS*, **534**, 1060
- Hatta Y., Sekii T., Takata M., Benomar O., 2021, *ApJ*, **923**, 244
- Henriksen A. I., et al., 2023a, *MNRAS*, **520**, 216
- Henriksen A. I., et al., 2023b, *MNRAS*, **524**, 4196
- Hidalgo J. P., Käpylä P. J., Schleicher D. R. G., Ortiz-Rodríguez C. A., Navarrete F. H., 2024, *A&A*, **691**, A326
- Huber D., et al., 2014, *ApJS*, **211**, 2
- Hubrig S., Järvinen S. P., Alvarado-Gómez J. D., Ilyin I., Schöller M., 2023, *MNRAS*, **526**, L83
- Jermyn A. S., Cantiello M., 2020, *ApJ*, **900**, 113
- Jermyn A. S., et al., 2023, *ApJS*, **265**, 15
- Kallinger T., Reegen P., Weiss W. W., 2008, *A&A*, **481**, 571
- Kiefer R., Schad A., Roth M., 2017, *ApJ*, **846**, 162
- Kovetz A., 1966, *ApJ*, **146**, 462
- Kurtz D. W., 1982, *MNRAS*, **200**, 807
- Kurtz D. W., 1990, *ARA&A*, **28**, 607
- Kurtz D. W., Saio H., Takata M., Shibahashi H., Murphy S. J., Sekii T., 2014, *MNRAS*, **444**, 102
- Landstreet J. D., 1982, *ApJ*, **258**, 639
- Lecoanet D., Vasil G. M., Fuller J., Cantiello M., Burns K. J., 2017, *MNRAS*, **466**, 2181
- Lecoanet D., Bowman D. M., Van Reeth T., 2022, *MNRAS*, **512**, L16
- Lee U., Baraffe I., 1995, *A&A*, **301**, 419
- Li G., Van Reeth T., Bedding T. R., Murphy S. J., Antoci V., Ouazzani R.-M., Barbara N. H., 2020, *MNRAS*, **491**, 3586
- Li G., Deheuvels S., Ballot J., Lignières F., 2022, *Nature*, **610**, 43
- Li G., Deheuvels S., Li T., Ballot J., Lignières F., 2023, *A&A*, **680**, A26
- Lignières F., Petit P., Aurière M., Wade G. A., Böhm T., 2014, in Petit P., Jardine M., Spruit H. C., eds, IAU Symposium Vol. 302, Magnetic Fields throughout Stellar Evolution. pp 338–347 ([arXiv:1402.5362](https://arxiv.org/abs/1402.5362)), doi:10.1017/S1743921314002440
- Loi S. T., 2020, *MNRAS*, **493**, 5726
- Lynden-Bell D., Ostriker J. P., 1967, *MNRAS*, **136**, 293
- Maeder A., 2009, Physics, Formation and Evolution of Rotating Stars. Astronomy and Astrophysics Library, Springer, Berlin Heidelberg, doi:10.1007/978-3-540-76949-1
- Mathis S., Bugnet L., 2023, *A&A*, **676**, L9
- Mathis S., Bugnet L., Prat V., Augustson K., Mathur S., García R. A., 2021, *A&A*, **647**, A122
- Mestel L., 2012, Stellar Magnetism, second edn. International Series of Monographs on Physics, Oxford University Press, Oxford
- Mestel L., Moss D. L., 1977, *MNRAS*, **178**, 27
- Miglio A., Montalbán J., Noels A., Eggenberger P., 2008, *MNRAS*, **386**, 1487
- Montgomery M. H., Metcalfe T. S., Winget D. E., 2003, *MNRAS*, **344**, 657
- Mosser B., et al., 2012, *A&A*, **537**, A30
- Mosser B., et al., 2017, *A&A*, **598**, A62
- Moyano F. D., Eggenberger P., Salmon S. J. A. J., Mombarg J. S. G., Ekström S., 2023, *A&A*, **677**, A6
- Moyano F. D., Eggenberger P., Salmon S. J. A. J., 2024, *A&A*, **681**, L16
- Murphy S. J., Moe M., Kurtz D. W., Bedding T. R., Shibahashi H., Boffin H. M. J., 2018, *MNRAS*, **474**, 4322
- Murphy S. J., Saio H., Takada-Hidai M., Kurtz D. W., Shibahashi H., Takata M., Hey D. R., 2020, *MNRAS*, **498**, 4272
- Neiner C., Geers V. C., Henrichs H. F., Floquet M., Frémat Y., Hubert A. M., Preuss O., Wiersma K., 2003, *A&A*, **406**, 1019
- Nemec J. M., Balona L. A., Murphy S. J., Kinemuchi K., Jeon Y.-B., 2017, *MNRAS*, **466**, 1290
- Paxton B., Bildsten L., Dotter A., Herwig F., Lesaffre P., Timmes F., 2011, *ApJS*, **192**, 3
- Paxton B., et al., 2013, *ApJS*, **208**, 4
- Paxton B., et al., 2015, *ApJS*, **220**, 15
- Paxton B., et al., 2018, *ApJS*, **234**, 34
- Paxton B., et al., 2019, *ApJS*, **243**, 10
- Petit V., Oksala M. E., 2025, *arXiv e-prints*, p. [arXiv:2504.00179](https://arxiv.org/abs/2504.00179)
- Petitdemange L., Marcotte F., Gissinger C., 2023, *Science*, **379**, 300
- Petitdemange L., Marcotte F., Gissinger C., Daniel F., 2024, *A&A*, **681**, A75
- Phinney R. A., Burridge R., 1973, *Geophysical Journal*, **34**, 451
- Prendergast K. H., 1956, *ApJ*, **123**, 498
- Ratnasingam R. P., Edelmann P. V. F., Bowman D. M., Rogers T. M., 2024, *ApJ*, **977**, L30
- Ritzwoller M. H., Lavelle E. M., 1991, *ApJ*, **369**, 557
- Roberts P. H., 1967, An Introduction to Magnetohydrodynamics. Longmans, London
- Rui N. Z., Fuller J., 2023, *MNRAS*, **523**, 582
- Saio H., 1981, *ApJ*, **244**, 299
- Saio H., Kurtz D. W., Takata M., Shibahashi H., Murphy S. J., Sekii T., Bedding T. R., 2015, *MNRAS*, **447**, 3264
- Schneider F. R. N., Ohlmann S. T., Podsiadlowski P., Röpeke F. K., Balbus S. A., Pakmor R., Springel V., 2019, *Nature*, **574**, 211
- Schou J., Christensen-Dalsgaard J., Thompson M. J., 1994, *ApJ*, **433**, 389
- Schwabe H., 1844, *Astronomische Nachrichten*, **21**, 233
- Shibahashi H., Takata M., 1993, *PASJ*, **45**, 617
- Shultz M. E., et al., 2019, *MNRAS*, **490**, 274
- Spruit H. C., 2002, *A&A*, **381**, 923
- Stępień K., 2000, *A&A*, **353**, 227
- Stello D., Cantiello M., Fuller J., Huber D., García R. A., Bedding T. R., Bildsten L., Silva Aguirre V., 2016, *Nature*, **529**, 364
- Stibbs D. W. N., 1950, *MNRAS*, **110**, 395
- Takada-Hidai M., Kurtz D. W., Shibahashi H., Murphy S. J., Takata M., Saio H., Sekii T., 2017, *MNRAS*, **470**, 4908
- Takata M., 2006, *PASJ*, **58**, 893
- Tayler R. J., 1973, *MNRAS*, **161**, 365
- Thomson-Paressant K., Neiner C., Lampens P., Labadie-Bartz J., Monier R., Mathias P., Tkachenko A., 2023, *MNRAS*, **526**, 1728
- Unno W., Osaki Y., Ando H., Saio H., Shibahashi H., 1989, Nonradial Oscillations of Stars, 2nd edn. University of Tokyo Press, Tokyo
- Wade G. A., et al., 2016, *MNRAS*, **456**, 2
- Woltjer L., 1960, *ApJ*, **131**, 227
- Zahn J. P., Brun A. S., Mathis S., 2007, *A&A*, **474**, 145



## APPENDIX A: ASYMMETRIC FREQUENCY SPLITTINGS OF HIGH-ORDER GRAVITY MODES CAUSED BY THE MAGNETIC FIELD

### A1 Guidelines of the analysis

We develop a regular perturbation analysis to obtain an expression for the frequency change of high-order and low-degree gravity modes due to slow rotation and a weak magnetic field that is confined in the stellar interior. Following [Li et al. \(2022\)](#), the present analysis is designed to be independent of the field configuration. One of our fundamental assumptions is that the rotation effect dominates over the magnetic effect. In this case, we may consider the rotation effect first, and then take the magnetic effect into account in the second step. An advantage of this approach is that the rotation perturbation lifts the degeneracy among the eigenmodes in the spherically symmetric case with respect to the azimuthal order,  $m$ , so that we may apply the non-degenerate perturbation theory in the second step. Then, the main point of the analysis is to calculate the matrix element of the magnetic operator. Since the expression for the matrix element can be highly complicated, we adopt its symmetric form (see [Kovetz 1966](#); [Glampedakis & Andersson 2007](#)). We list two advantages of this approach: (1) the variational principle can be applied; (2) the frequency perturbations are clearly real.

In general, the magnetic effect consists of two aspects. Firstly, the equilibrium structure is deformed by the Lorentz force. This structure change contributes to the frequency change. Then, oscillations occur about the deformed structure under the direct influence of the Lorentz force. Following [Gough & Thompson \(1990\)](#), we refer to the former and the latter as the indirect and direct effects, respectively.

### A2 Oscillation equations in the presence of the magnetic field

We start from the equation of motion of a uniformly rotating magnetized fluid in the rotating frame,

$$\rho \frac{d\mathbf{v}}{dt} = -\nabla p - \rho \nabla \Phi + \frac{1}{c_*} \mathbf{j} \times \mathbf{B} - \rho [2\boldsymbol{\Omega} \times \mathbf{v} + \boldsymbol{\Omega} \times (\boldsymbol{\Omega} \times \mathbf{r})] , \quad (\text{A1})$$

in which  $d/dt$  is the Lagrangian time derivative,  $\mathbf{v}$  the velocity,  $p$  the pressure,  $\Phi$  the gravitational potential,  $c_*$  the speed of light in vacuum,  $\mathbf{j}$  the electric current density,  $\mathbf{B}$  the magnetic field,  $\boldsymbol{\Omega}$  the rotation vector and  $\mathbf{r}$  the position vector. The third term on the right-hand side of equation (A1) stands for the Lorentz force, while the fourth and fifth terms represent the Coriolis and centrifugal forces, respectively. We assume that  $\mathbf{j}$  is related to  $\mathbf{B}$  by Ampere's law (or the Ampere–Maxwell equation neglecting the displacement current),

$$\nabla \times \mathbf{B} = \frac{4\pi}{c_*} \mathbf{j} . \quad (\text{A2})$$

Equation (A1) can be recast as

$$\rho \frac{dv_i}{dt} = -\partial_j \Pi_{j,i} - \rho \partial_i \Psi - 2\rho (\boldsymbol{\Omega} \times \mathbf{v})_i , \quad (\text{A3})$$

where subscripts  $i$  and  $j$  mean the  $i$ -th and  $j$ -th components of the Cartesian coordinates, respectively. We follow the Einstein summation convention for repeated indices. In equation (A3), tensor  $\Pi_{i,j}$  and scalar  $\Psi$  are introduced by

$$\Pi_{i,j} \equiv \delta_{i,j} \left( p + \frac{\mathbf{B}^2}{8\pi} \right) - \frac{B_i B_j}{4\pi} \quad (\text{A4})$$

and

$$\Psi = \Phi - \frac{1}{2} |\boldsymbol{\Omega} \times \mathbf{r}|^2 . \quad (\text{A5})$$

In equation (A4),  $\delta_{i,j}$  is the Kronecker delta. Assuming that there is no velocity field in the equilibrium structure (in the rotating frame), we can linearize equation (A3) to derive the oscillation equation with respect to a small displacement vector  $\boldsymbol{\xi}$ ,

$$\sigma^2 \rho \xi_i = \sigma C_{i,j} \xi_j + T_{i,j} \xi_j , \quad (\text{A6})$$

in which we have assumed that  $\boldsymbol{\xi}$  depends on time  $t$  as  $\exp(-i\sigma t)$  with an angular frequency  $\sigma$ . The tensorial operators  $T_{i,j}$  and  $C_{i,j}$  in equation (A6) are defined by

$$T_{i,j} \xi_j \equiv \rho \delta \left( \frac{1}{\rho} \partial_j \Pi_{j,i} \right) + \rho \delta (\partial_i \Psi) \quad (\text{A7})$$

and

$$C_{i,j} \xi_j \equiv -2i\rho (\boldsymbol{\Omega} \times \boldsymbol{\xi})_i . \quad (\text{A8})$$

In equation (A7),  $\delta$  is the operator for the Lagrangian perturbation. In order to relate the perturbed quantities in equation (A7) to  $\boldsymbol{\xi}$ , we need to use the linearized versions of the continuity equation, the Poisson equation and the adiabatic relation between the Lagrangian pressure and density perturbations. In addition, we also use the linearized induction equation of (ideal) magnetohydrodynamics,

$$\delta \mathbf{B} [\boldsymbol{\xi}] = (\mathbf{B} \cdot \nabla) \boldsymbol{\xi} - (\nabla \cdot \boldsymbol{\xi}) \mathbf{B} \quad (\text{A9})$$

(e.g. [Roberts 1967](#)).

### A3 Matrix element

It can be shown that the operator  $T_{i,j}$  is symmetric in the sense,

$$\mathcal{T}(\hat{\boldsymbol{\xi}}, \boldsymbol{\xi}) = \left[ \mathcal{T}(\boldsymbol{\xi}, \hat{\boldsymbol{\xi}}) \right]^* , \quad (\text{A10})$$

where  $*$  indicates the complex conjugate. Here,  $\mathcal{T}$  is defined by

$$\mathcal{T}(\hat{\boldsymbol{\xi}}, \boldsymbol{\xi}) \equiv \int \hat{\xi}_i^* T_{i,j} \xi_j dV , \quad (\text{A11})$$

in which the domain of the integral is the entire stellar volume. Equation (A10) holds for any  $\boldsymbol{\xi}$  and  $\hat{\boldsymbol{\xi}}$  that satisfy the proper boundary conditions. The proof is almost the same as that given by [Kovetz \(1966\)](#), except that  $\Phi$  should be replaced with  $\Psi$ . Since  $C_{i,j}$  is also symmetric ([Lynden-Bell & Ostriker 1967](#)), the total operator  $\sigma C_{i,j} + T_{i,j}$  on the right-hand side of equation (A6) is symmetric as a whole. This property serves as a basis of the variational principle.

The symmetric form of  $\mathcal{T}$  is composed of three parts,

$$\mathcal{T}(\hat{\boldsymbol{\xi}}, \boldsymbol{\xi}) = \mathcal{L}(\hat{\boldsymbol{\xi}}, \boldsymbol{\xi}) + \mathcal{B}(\hat{\boldsymbol{\xi}}, \boldsymbol{\xi}) + \mathcal{R}(\hat{\boldsymbol{\xi}}, \boldsymbol{\xi}) . \quad (\text{A12})$$

Here,  $\mathcal{L}$  and  $\mathcal{B}$  correspond to the part that does not depend on  $\mathbf{B}$  directly, and that explicitly includes it, respectively, while  $\mathcal{R}$  stands for the contribution coming from the surface and the exterior of the star. They are further decomposed as

$$\mathcal{L}(\hat{\boldsymbol{\xi}}, \boldsymbol{\xi}) = \mathcal{S}_L(\hat{\boldsymbol{\xi}}, \boldsymbol{\xi}) + \mathcal{A}_L(\hat{\boldsymbol{\xi}}, \boldsymbol{\xi}) + \left[ \mathcal{A}_L(\boldsymbol{\xi}, \hat{\boldsymbol{\xi}}) \right]^* , \quad (\text{A13})$$

$$\mathcal{B}(\hat{\boldsymbol{\xi}}, \boldsymbol{\xi}) = \mathcal{S}_B(\hat{\boldsymbol{\xi}}, \boldsymbol{\xi}) + \mathcal{A}_B(\hat{\boldsymbol{\xi}}, \boldsymbol{\xi}) + \left[ \mathcal{A}_B(\boldsymbol{\xi}, \hat{\boldsymbol{\xi}}) \right]^* \quad (\text{A14})$$

and

$$\mathcal{R}(\hat{\boldsymbol{\xi}}, \boldsymbol{\xi}) = \mathcal{S}_R(\hat{\boldsymbol{\xi}}, \boldsymbol{\xi}) + \mathcal{A}_R(\hat{\boldsymbol{\xi}}, \boldsymbol{\xi}) + \left[ \mathcal{A}_R(\boldsymbol{\xi}, \hat{\boldsymbol{\xi}}) \right]^* , \quad (\text{A15})$$

where  $\mathcal{S}$  and  $\mathcal{A}$  mean the symmetric and asymmetric parts, respectively. The definitions of  $\mathcal{S}_L$ ,  $\mathcal{A}_L$ ,  $\mathcal{S}_B$ ,  $\mathcal{A}_B$ ,  $\mathcal{S}_R$  and  $\mathcal{A}_R$  are provided



by

$$S_L(\hat{\xi}, \xi) \equiv \int \Gamma_1 p (\nabla \cdot \hat{\xi}^*) (\nabla \cdot \xi) dV - G \iint \left[ \rho(r_a) \hat{\xi}^*(r_a) \cdot \nabla_a \right] \left[ \rho(r_b) \xi(r_b) \cdot \nabla_b \right] \times \left( \frac{1}{|r_a - r_b|} \right) dV_a dV_b, \quad (\text{A16})$$

$$\mathcal{A}_L(\hat{\xi}, \xi) \equiv - \int (\hat{\xi}^* \cdot \nabla \Psi) \left( \rho \nabla \cdot \xi + \frac{1}{2} \xi \cdot \nabla \rho \right) dV, \quad (\text{A17})$$

$$S_B(\hat{\xi}, \xi) \equiv \frac{1}{4\pi} \int \delta \mathbf{B} [\hat{\xi}^*] \cdot \delta \mathbf{B} [\xi] dV, \quad (\text{A18})$$

$$\mathcal{A}_B(\hat{\xi}, \xi) \equiv \frac{1}{4\pi} \int \left[ (\nabla \cdot \hat{\xi}^*) (\xi \cdot [(\mathbf{B} \cdot \nabla) \mathbf{B}]) + \frac{1}{2} \hat{\xi}^* \cdot \{(\xi \cdot \nabla) [(\mathbf{B} \cdot \nabla) \mathbf{B}]\} \right] dV, \quad (\text{A19})$$

$$S_R(\hat{\xi}, \xi) \equiv \int (\mathbf{n} \cdot \hat{\xi}^*) (\mathbf{n} \cdot \xi) (\mathbf{n} \cdot \nabla) \left[ \frac{\mathbf{B}_{\text{ex}}^2}{8\pi} - \left( p + \frac{\mathbf{B}^2}{8\pi} \right) \right] dS + \int_{V_{\text{ex}}} \frac{\mathbf{B}'_{\text{ex}} [\hat{\xi}^*] \cdot \mathbf{B}'_{\text{ex}} [\xi]}{4\pi} dV \quad (\text{A20})$$

and

$$\mathcal{A}_R(\hat{\xi}, \xi) \equiv - \frac{1}{8\pi} \int (\mathbf{n} \cdot \mathbf{B}) \hat{\xi}^* \cdot [(\xi \cdot \nabla) \mathbf{B}_{\text{ex}}] dS. \quad (\text{A21})$$

In equation (A16),  $\Gamma_1$  is the first adiabatic index, while  $\mathbf{n}$  in equation (A20) is the unit normal vector of the stellar surface. In equations (A20) and (A21),  $\mathbf{B}_{\text{ex}}$  and  $\mathbf{B}'_{\text{ex}}[\xi]$  mean the magnetic field in the exterior of the star and its Eulerian perturbation that is induced by displacement  $\xi$  in the interior. The volume integral in equation (A20) is performed over the whole region outside the star, while the surface integrals in equations (A20) and (A21) are over the entire surface of the star. When we derive equations (A16)–(A19), we have used the equilibrium relation,

$$-\nabla \left( p + \frac{\mathbf{B}^2}{8\pi} \right) + \frac{(\mathbf{B} \cdot \nabla) \mathbf{B}}{4\pi} - \rho \nabla \Psi = 0. \quad (\text{A22})$$

Utilizing this relation, we can show that equation (A12) is equivalent to equation (39) of Kovetz (1966).<sup>3</sup>

In addition to the absence of the magnetic field at the surface and the exterior, we also assume that the density is equal to zero at the surface in the equilibrium structure. Under these assumptions, we simply obtain

$$\mathcal{R}(\hat{\xi}, \xi) = 0. \quad (\text{A23})$$

#### A4 Frequency perturbation

Equation (A6) is a general expression that assumes neither slow rotation nor a weak magnetic field. The next step is to regard them as small perturbations. Although equation (A6) concerns oscillations about the (rotationally and magnetically) deformed equilibrium structure, we may reinterpret this equation as describing oscillations about the

non-rotating and non-magnetic structure with two different kinds of perturbations, the contributions to the restoring force and the deformation. Since we consider the major effect of rotation separately in the first step, we study here the frequency perturbation due only to the magnetic effect. We can then separate the quantities in equation (A6) into the unperturbed part (with subscript 0) and the perturbed part (with subscript 1). Thanks to the symmetric property of  $T_{i,j}$ , we can derive an expression for the frequency perturbation as

$$\sigma_1 = \frac{\mathcal{T}_1(\xi_0, \xi_0) - \sigma_0^2 \int \rho_1 |\xi_0|^2 dV}{2\sigma_0 \mathcal{I}(\xi_0, \xi_0)}, \quad (\text{A24})$$

in which we have introduced

$$\mathcal{I}(\hat{\xi}, \xi) \equiv \int \rho_0 \hat{\xi}^* \cdot \xi dV. \quad (\text{A25})$$

We implicitly assume in equation (A24) that the third- and higher-order effects of rotation are negligible. Strictly speaking, as we explain in Appendix A1, the unperturbed eigenfunctions should be those after taking the rotation effect into account. However, since we analyse only the leading-order effect, we may neglect the perturbation to  $\xi_0$  due to rotation, and adopt as  $\xi_0$  the eigenfunctions of the spherically symmetric structure. In this case,  $\xi_0$  can be expressed in the spherical coordinates  $(r, \theta, \phi)$  with the origin ( $r = 0$ ) set at the centre of the star and the direction of  $\theta = 0$  aligned with the rotation axis as

$$\xi_0 = \xi_r(r) Y_\ell^m(\theta, \phi) \mathbf{e}_r + \xi_h(r) \nabla_\perp Y_\ell^m(\theta, \phi), \quad (\text{A26})$$

in which  $Y_\ell^m(\theta, \phi)$  is the spherical harmonic with the angular degree  $\ell$  and the azimuthal order  $m$ . While  $\mathbf{e}_r$  is the unit vector in the radial direction, the horizontal gradient operator  $\nabla_\perp$  is defined by

$$\nabla_\perp = \mathbf{e}_\theta \frac{\partial}{\partial \theta} + \mathbf{e}_\phi \frac{1}{\sin \theta} \frac{\partial}{\partial \phi}, \quad (\text{A27})$$

where  $\mathbf{e}_\theta$  and  $\mathbf{e}_\phi$  are the unit vectors in the  $\theta$  and  $\phi$  directions, respectively. The functions  $\xi_r$  and  $\xi_h$  depend not only on  $r$  but also on  $\ell$  and the radial order  $n$ . The corresponding eigenfrequency  $\sigma_0$  is also dependent on  $n$  and  $\ell$ .

The matrix element  $\mathcal{T}_1(\xi_0, \xi_0)$  is obtained by perturbing equation (A12) as

$$\mathcal{T}_1(\xi_0, \xi_0) = \mathcal{L}_1(\xi_0, \xi_0) + \mathcal{B}(\xi_0, \xi_0), \quad (\text{A28})$$

in which  $\mathcal{L}_1$  can in turn be derived by perturbing equation (A13) as

$$\mathcal{L}_1(\xi_0, \xi_0) = S_{L,1}(\xi_0, \xi_0) + 2\mathcal{R}[\mathcal{A}_{L,1}(\xi_0, \xi_0)]. \quad (\text{A29})$$

Here,  $S_{L,1}$  and  $\mathcal{A}_{L,1}$  are provided by

$$S_{L,1}(\xi_0, \xi_0) \equiv \int (\Gamma_1 p)_1 |\nabla \cdot \xi_0|^2 dV - 2G \mathcal{R} \left\{ \iint \left[ \rho_0(r_a) \xi_0^*(r_a) \cdot \nabla_a \right] \left[ \rho_1(r_b) \xi_0(r_b) \cdot \nabla_b \right] \times \left( \frac{1}{|r_a - r_b|} \right) dV_a dV_b \right\} \quad (\text{A30})$$

and

$$\mathcal{A}_{L,1}(\xi_0, \xi_0) \equiv - \int \left\{ (\xi_0^* \cdot \nabla \Phi_1) \left( \rho_0 \nabla \cdot \xi_0 + \frac{1}{2} \xi_0 \cdot \nabla \rho_0 \right) + (\xi_0^* \cdot \nabla \Phi_0) \left( \rho_1 \nabla \cdot \xi_0 + \frac{1}{2} \xi_0 \cdot \nabla \rho_1 \right) \right\} dV. \quad (\text{A31})$$

In equation (A28),  $\mathcal{B}$  corresponds to the direct effect of the magnetic field, while  $\mathcal{L}_1$  and the second term in the numerator of equation (A24) describe the indirect effect.

<sup>3</sup> For comparison, we need to replace  $U$  with  $-\Psi$  in the equation. In addition, we believe that in Kovetz (1966) the second term in the fourth line has a sign error, and that  $B^2/(8\rho)$  in the sixth line means  $B^2/(8\pi)$ .

### A5 Dominant terms for high-order and low-degree gravity modes

We evaluate equation (A24) for high-order and low-degree gravity modes. A primary parameter is

$$\epsilon = \frac{\sigma_0}{N(r_*)} \ll 1, \quad (\text{A32})$$

in which  $r_*$  is a representative radius in the propagative region of gravity waves. We also assume that

$$\frac{\sigma_0 r_*}{c} \ll 1, \quad (\text{A33})$$

in which  $c$  is the sound speed. According to the asymptotic analysis (e.g. [Unno et al. 1989](#)), the horizontal displacement  $\xi_h$  dominates over the radial displacement  $\xi_r$  by factor  $\epsilon^{-1}$ . Because the wavelength at radius  $r$  is on the order of  $\epsilon r$ , the first derivatives of the eigenfunctions  $\xi$  with respect to  $r$  are evaluated to be  $\sim \epsilon^{-1} r^{-1} \xi$ . Exceptionally, the divergence,  $\nabla \cdot \xi$ , is only on the order of  $r^{-1} \xi_r$ , which reflects that high-order gravity waves are almost uncompressed.

As for the field configuration, we assume

$$\epsilon \lesssim \frac{|B_r|}{|B_\phi|} \ll 1 \quad (\text{A34})$$

and  $|B_\theta| \sim |B_\phi|$ , the latter of which will be changed at the last step.

Under these assumptions, we retain only the terms that can be on the order of  $\epsilon^{-2} \xi_h^2 B_r^2$  or  $\xi_h^2 B_\theta^2$  or  $\xi_h^2 B_\phi^2$  in the numerator on the right-hand side of equation (A24). We may thus identify the dominant terms in  $\mathcal{B}(\xi_0, \xi_0)$  as

$$\mathcal{B}(\xi_0, \xi_0) \approx \frac{1}{4\pi} \int \left( |(\mathbf{B} \cdot \nabla) \xi_0|^2 + \Re [\xi_0^* \cdot \{(\xi_0 \cdot \nabla) [(\mathbf{B} \cdot \nabla) \mathbf{B}]\}] \right) dV, \quad (\text{A35})$$

and confirm that there is no contribution from  $\mathcal{L}_1(\xi_0, \xi_0)$  and the second term in the numerator of equation (A24). This means that the indirect effects of the magnetic field is not important for high-order gravity modes even in the order that we consider in the present analysis (see [Mathis & Bugnet 2023](#)). As a result, equation (A24) is reduced to

$$\sigma_1 \approx \frac{\mathcal{B}(\xi_0, \xi_0)}{2\sigma_0 \mathcal{I}(\xi_0, \xi_0)}. \quad (\text{A36})$$

We remark on the second term on the right-hand side of equation (A30), which appears to be on the order of  $\xi_h^2 B_\phi^2$ . However, this integral includes the Eulerian perturbation to the gravitational potential,  $\Phi'_\xi$ , which is given by

$$\Phi'_\xi(\mathbf{r}) = -G \int \rho(\mathbf{r}_a) \xi(\mathbf{r}_a) \cdot \nabla_a \left( \frac{1}{|\mathbf{r} - \mathbf{r}_a|} \right) dV_a. \quad (\text{A37})$$

It is well established that  $\Phi'_\xi$  is negligibly small for high-order gravity modes ([Cowling 1941](#)).

### A6 Evaluation of the dominant terms

#### A6.1 Angular integrals

The main result of this section is the expression for the angular integral in equation (A35), which is provided by

$$\begin{aligned} & \int_{4\pi} \left( |(\mathbf{B} \cdot \nabla) \xi_0|^2 + \Re [\xi_0^* \cdot \{(\xi_0 \cdot \nabla) [(\mathbf{B} \cdot \nabla) \mathbf{B}]\}] \right) d\Omega \\ & \approx \left( \frac{d\xi_h}{dr} \right)^2 \int_{4\pi} B_r^2 D_\ell^m d\Omega + \left( \frac{\xi_h}{r} \right)^2 \int_{4\pi} \left( B_\theta^2 F_\ell^m + B_\phi^2 G_\ell^m \right) d\Omega, \end{aligned} \quad (\text{A38})$$

where  $D_\ell^m$ ,  $F_\ell^m$  and  $G_\ell^m$  are all functions of  $\theta$ . In equation (A38),  $d\Omega$  means an infinitesimal element of a solid angle, given by  $d\Omega = \sin \theta d\theta d\phi$ . Their derivation is lengthy, but straightforward if we use generalised spherical harmonics ([Gel'fand & Šapiro 1956](#)), which are widely used in geophysics (e.g. [Phinney & Burridge 1973](#); [Dahlen & Tromp 1998](#)) and have also been adapted to helio- and asteroseismic problems (e.g. [Ritzwoller & Lavelly 1991](#); [Hanasoge et al. 2017](#); [Kiefer et al. 2017](#); [Das et al. 2020](#)). The results are summarised as follows:

$$D_\ell^m = \sum_{k=0}^{\ell} U_{\ell,k} (K - 2L) \mathcal{P}_{2k}^{(\ell)}(m) P_{2k}(\cos \theta), \quad (\text{A39})$$

$$\begin{aligned} \frac{F_\ell^m + G_\ell^m}{2} &= \sum_{k=0}^{\ell} U_{\ell,k} \left[ -(K - 2L)(K + 1) - 2L^2 \right] \\ &\times \mathcal{P}_{2k}^{(\ell)}(m) P_{2k}(\cos \theta) \end{aligned} \quad (\text{A40})$$

and

$$\begin{aligned} \frac{F_\ell^m - G_\ell^m}{2} &= \sum_{k=1}^{\ell} U_{\ell,k} \frac{K(K + 2L - 1) - 4L(L + 1)}{4(K - 1)} \\ &\times \mathcal{P}_{2k}^{(\ell)}(m) P_{2k}^2(\cos \theta), \end{aligned} \quad (\text{A41})$$

in which we have introduced

$$U_{\ell,k} \equiv (-1)^{k+1} \frac{(4k + 1)(2k)!(2\ell + 1)!(\ell + k)!}{4\pi\ell(k!)^2(2\ell + 2k + 1)!(\ell - k)!}, \quad (\text{A42})$$

$$K \equiv k(2k + 1), \quad (\text{A43})$$

$$L \equiv \frac{\ell(\ell + 1)}{2} \quad (\text{A44})$$

and

$$\mathcal{P}_j^{(\ell)}(m) \equiv (-1)^{-\ell+m} \frac{\ell \sqrt{(2\ell - j)!(2\ell + j + 1)!}}{(2\ell)!} \begin{pmatrix} \ell & \ell & j \\ m & -m & 0 \end{pmatrix}. \quad (\text{A45})$$

Note that  $P_{2k}$  in equations (A39) and (A40) are the Legendre polynomials, while  $P_{2k}^2$  in equation (A41) are the associated Legendre functions. The last factor on the right-hand side of equation (A45) is Wigner's 3- $j$  symbol. The coefficients  $\mathcal{P}_j^{(\ell)}(m)$  are polynomials in  $m$  of degree  $j$ , which form a basis to represent the frequency splitting as

$$\nu(n, \ell, m) = \sum_{j=0}^{2\ell} a_j(n, \ell) \mathcal{P}_j^{(\ell)}(m). \quad (\text{A46})$$

Here,  $a_j$  is called the a-coefficient of order  $j$ . The asymmetry in the frequency splittings defined by equation (1) is related to  $a_2$  as

$$a_n = 3a_2(n, 1). \quad (\text{A47})$$

The coefficients  $\mathcal{P}_j^{(\ell)}(m)$  are first introduced by [Ritzwoller & Lavelly \(1991\)](#) to analyse frequency splittings in the spectrum of solar oscillations, while they are also used in asteroseismic analyses (e.g. [Benomar et al. 2023](#)). Here, we adopt the normalization introduced by [Schou et al. \(1994\)](#). It is worth noting the following relation:

$$U_{\ell,k} \mathcal{P}_{2k}^{(\ell)}(m) = -\sqrt{\frac{4k + 1}{4\pi}} \int_{4\pi} Y_{2k}^0 |Y_\ell^m|^2 d\Omega. \quad (\text{A48})$$

The expressions for  $D_\ell^m$ ,  $F_\ell^m$  and  $G_\ell^m$  are given for  $\ell = 1$  and 2 as follows:

$$D_1^m = \frac{1}{2\pi} + \frac{1}{8\pi} \mathcal{P}_2^{(1)}(m) (3 \cos^2 \theta - 1), \quad (\text{A49})$$

$$F_1^m = \frac{3}{8\pi} \mathcal{P}_2^{(1)}(m) (3 - 7 \cos^2 \theta), \quad (\text{A50})$$

$$G_1^m = \frac{3}{8\pi} \mathcal{P}_2^{(1)}(m) (1 - 5 \cos^2 \theta), \quad (\text{A51})$$

$$D_2^m = \frac{3}{2\pi} - \frac{15}{28\pi} \mathcal{P}_2^{(2)}(m) P_2(\cos \theta) - \frac{3}{14\pi} \mathcal{P}_4^{(2)}(m) P_4(\cos \theta), \quad (\text{A52})$$

$$\begin{aligned} \frac{F_2^m + G_2^m}{2} &= \frac{3}{\pi} - \frac{15}{14\pi} \mathcal{P}_2^{(2)}(m) P_2(\cos \theta) \\ &+ \frac{93}{28\pi} \mathcal{P}_4^{(2)}(m) P_4(\cos \theta) \end{aligned} \quad (\text{A53})$$

$$\begin{aligned} \text{and} \\ \frac{F_2^m - G_2^m}{2} &= -\frac{15}{28\pi} \mathcal{P}_2^{(2)}(m) P_2^2(\cos \theta) \\ &- \frac{17}{112\pi} \mathcal{P}_4^{(2)}(m) P_4^2(\cos \theta), \end{aligned} \quad (\text{A54})$$

in which  $\mathcal{P}_j^{(\ell)}(m)$  coefficients are provided by

$$\mathcal{P}_2^{(1)}(m) = 3m^2 - 2 \quad (\text{A55})$$

$$\mathcal{P}_2^{(2)}(m) = m^2 - 2 \quad (\text{A56})$$

and

$$\mathcal{P}_4^{(2)}(m) = \frac{35m^4 - 155m^2 + 72}{6}. \quad (\text{A57})$$

Note that  $D_\ell^m$ ,  $F_\ell^m$  and  $G_\ell^m$  depend on  $m$  only through  $\mathcal{P}_{2k}^{(\ell)}(m)$ , which include only even powers of  $m$ . The independence of the sign of  $m$  comes from the symmetric property of the operator  $\mathcal{B}$  (see equation (A14)).

## A6.2 Radial integrals

In order to evaluate  $\xi_h$  in equation (A38), we use its asymptotic expression,

$$\xi_h \approx A \left( \frac{N}{\sigma_0^3 \rho r^3} \right)^{1/2} \sin \left( \int_{r_{\text{in}}}^r k_r dr - \varphi_{\text{in}} \right), \quad (\text{A58})$$

in which  $A$  is a normalisation constant,  $r_{\text{in}}$  the inner turning point of the gravity-mode cavity,  $\varphi_{\text{in}}$  the phase lag introduced at  $r = r_{\text{in}}$  and  $k_r$  defined by

$$k_r \equiv \frac{\sqrt{\ell(\ell+1)N}}{\sigma_0 r} \quad (\text{A59})$$

(e.g. [Unno et al. 1989](#)). We accordingly obtain

$$\frac{d\xi_h}{dr} \approx A \left( \frac{\ell(\ell+1)N^3}{\sigma_0^5 \rho r^5} \right)^{1/2} \cos \left( \int_{r_{\text{in}}}^r k_r dr - \varphi_{\text{in}} \right). \quad (\text{A60})$$

When we evaluate the radial integrals that include  $\xi_h^2$  or  $(d\xi_h/dr)^2$ , the highly oscillatory factors proportional to  $\sin^2$  and  $\cos^2$  can be replaced with 1/2, and the domain of integrals can be set to  $G_B$ . We

may thus calculate equation (A35) as

$$\begin{aligned} \mathcal{B}(\xi_0, \xi_0) &\approx \frac{A^2 \ell(\ell+1)}{8\pi \sigma_0^5} \int_{G_B} \frac{N^3}{\rho r^3} \int_{4\pi} B_r^2 D_\ell^m d\Omega dr \\ &+ \frac{A^2}{8\pi \sigma_0^3} \int_{G_B} \frac{N}{\rho r^3} \int_{4\pi} (B_\theta^2 F_\ell^m + B_\phi^2 G_\ell^m) d\Omega dr. \end{aligned} \quad (\text{A61})$$

Similarly, we may compute  $\mathcal{I}(\xi_0^*, \xi_0)$  in equation (A25) as

$$\begin{aligned} \mathcal{I}(\xi_0, \xi_0) &= \int [\xi_r^2 + \ell(\ell+1)\xi_h^2] \rho r^2 dr \approx \ell(\ell+1) \int \rho r^2 \xi_h^2 dr \\ &\approx \frac{A^2 \ell(\ell+1)}{2\sigma_0^3} \int_G \frac{N}{r} dr. \end{aligned} \quad (\text{A62})$$

Using equations (A61) and (A62) in equation (A36), we obtain the expression for the magnetic perturbation to cyclic frequency as

$$\begin{aligned} \nu_1 &= \left( \int_G \frac{N}{r} dr \right)^{-1} \left[ \frac{1}{128\pi^5 \nu_0^3} \int_{G_B} \frac{N^3}{\rho r^3} \int_{4\pi} B_r^2 D_\ell^m d\Omega dr \right. \\ &\quad \left. + \frac{1}{32\pi^3 \ell(\ell+1) \nu_0} \int_{G_B} \frac{N}{\rho r^3} \int_{4\pi} (B_\theta^2 F_\ell^m + B_\phi^2 G_\ell^m) d\Omega dr \right]. \end{aligned} \quad (\text{A63})$$

## A7 Asymmetry of the frequency splittings of dipolar modes

We derive the expression for the asymmetry of the frequency splittings for  $\ell = 1$ . Using equations (A49)–(A51), we first obtain

$$D_1^1 - D_1^0 = \frac{3}{8\pi} (3 \cos^2 \theta - 1) \equiv \frac{3}{4\pi} W_r(\cos \theta), \quad (\text{A64})$$

$$F_1^1 - F_1^0 = -\frac{9}{8\pi} (7 \cos^2 \theta - 3) \equiv -\frac{9}{2\pi} W_\theta(\cos \theta) \quad (\text{A65})$$

and

$$G_1^1 - G_1^0 = -\frac{9}{8\pi} (5 \cos^2 \theta - 1) \equiv -\frac{9}{2\pi} W_\phi(\cos \theta), \quad (\text{A66})$$

where  $W_\alpha(\cos \theta)$  with  $\alpha = r, \theta$  and  $\phi$  are normalised so that they take their maxima of  $W_\alpha = 1$  at  $\theta = 0$ . Noting that the asymmetry is equal to the difference in frequency perturbation between  $m = 1$  and  $m = 0$  with the same radial order  $n$  and the spherical degree  $\ell = 1$ , we obtain its expression from equations (A63)–(A66) as

$$\begin{aligned} \alpha_n^{(\text{mag})} &= \left( \int_G \frac{N}{r} dr \right)^{-1} \left( \frac{3}{128\pi^5 \nu_{n,1}^3} \int_{G_B} \frac{N^3}{\rho r^3} \overline{W_r B_r^2} dr \right. \\ &\quad \left. - \frac{9}{32\pi^3 \nu_{n,1}} \int_{G_B} \frac{N}{\rho r^3} \overline{W_\theta B_\theta^2 + W_\phi B_\phi^2} dr \right), \end{aligned} \quad (\text{A67})$$

in which overlines mean the spherical averages (see equation (12)). Equation (A67) is equivalent to equation (6), if we assume  $|B_\theta| \ll |B_\phi|$ .

## A8 Validity condition of the perturbation analysis

The perturbation analysis presented in this paper can be justified only if the magnetic effect is a small perturbation. This condition can be rephrased as the perturbed Lorentz force being much smaller than the total restoring force that exists in the absence of the magnetic field. For high-order gravity modes, the dominant force is the buoyancy force, which is always in the radial direction, whereas only the Eulerian perturbation to the pressure gradient ( $\nabla p'$ ) contributes to the horizontal component of the total force. We first derive the condition

of the horizontal component of the Lorentz force  $\mathbf{L}'$  being much smaller than that of  $\nabla p'$ . We then discuss the condition about the radial components.

The horizontal component of  $\nabla p'$  can be estimated from the perturbed equation of motion to be

$$(\nabla p')_{\perp} = \frac{p'}{r} \nabla_{\perp} Y_{\ell}^m \approx \sigma^2 \rho \xi_h \nabla_{\perp} Y_{\ell}^m, \quad (\text{A68})$$

in the Cowling approximation. On the other hand, the dominant horizontal component of the Lorentz force is given for high-order gravity modes by

$$\mathbf{L}'_{\perp} \approx -\frac{1}{4\pi} B_r^2 k_r^2 \xi_h \nabla_{\perp} Y_{\ell}^m \quad (\text{A69})$$

(see equation (A35)). Here, we do not assume equation (A34), but consider that all of the components of  $\mathbf{B}$  are on the same order, which does not seriously influence the order-of-magnitude estimate in this section.

From equations (A68) and (A69), we may introduce a dimensionless parameter to measure the importance of the Lorentz force by

$$s_m \equiv \left( \frac{B_r}{B_r^{\text{UL}}} \right)^2, \quad (\text{A70})$$

in which  $B_r^{\text{UL}}$  is defined by

$$B_r^{\text{UL}} \equiv \sqrt{\frac{4\pi\rho}{\ell(\ell+1)} \frac{\sigma^2 r}{N}}. \quad (\text{A71})$$

If we do not take the rotation into account, the condition for the magnetic field to be weak enough to apply the perturbation analysis is given simply by  $s_m \ll 1$ , or equivalently  $|B_r| \ll B_r^{\text{UL}}$ . The upper limit given by equation (A71) is essentially the same as that derived by Bugnet et al. (2021) in their equation (29) and larger by factor two than the critical field strength in equation (3) of Fuller et al. (2015) for  $\ell = 1$ .

We now turn to the radial components. Since  $\mathbf{L}'$  is perpendicular to  $\mathbf{B}$ , the radial component of  $\mathbf{L}'$  is different in amplitude from its horizontal component by at most factor

$$f_L = \left| \frac{B_{\perp}}{B_r} \right|, \quad (\text{A72})$$

in which  $B_{\perp}$  means the amplitude of the horizontal component of  $\mathbf{B}$ . On the other hand, the buoyancy force  $\rho N^2 \xi_r$  is larger than  $|(\nabla p')_{\perp}|$  by factor

$$f_N = \frac{N}{\sigma} \quad (\text{A73})$$

for high-order gravity modes. Therefore, in the situations where  $f_L \lesssim f_N$ , the buoyancy force dominates over the radial component of  $\mathbf{L}'$  if equation (A70) is satisfied. In fact, from Table 4 of this paper and Fig. 12 of S15, we estimate  $(f_L, f_N) \sim (26, 10\text{--}100)$  for  $r/R \lesssim 0.5$ .

## APPENDIX B: ASPHERICAL BUOYANCY GLITCHES

### B1 Background

Physical processes in the stellar interior often create a layer of rapid variation in chemical composition and other physical quantities typically near the boundary of mixing regions. If the scale height of the variation is much shorter than the wavelength of waves that go through the layer, the structure is essentially considered as a discontinuous surface, which generally disturbs the wave propagation, and

hence modifies the frequencies of modes that consist of those waves. This is called a glitch problem in asteroseismology. The problem is particularly important for high-order modes because the glitch induces characteristic signatures in the spectrum of mode frequencies (or periods) depending on its structure. Such signatures, which are frequently observed in real stars, provide us with a unique probe into the properties of the physical processes that cause the glitch.

In this appendix, we confine ourselves to the glitch problem of high-order gravity modes, for which a considerable amount of effort has already been made. The present analysis extends it to take account of the glitch structure that is not spherically symmetric. For simplicity, we assume that the discontinuity is so weak that we may apply the variational principle (or the perturbation theory in the non-degenerate case) to estimate the change in the mode frequencies (or periods). This also implies another assumption that the degeneracy among the modes with the same radial order and the same spherical degree, but with different azimuthal orders, has been lifted by the effect of the rotation before we consider a smaller effect of the glitch (see appendix A1).

### B2 Framework for high-order gravity modes with uniform rotation

Under the assumptions that we have made, our task is simply to evaluate equation (A24) without taking the magnetic field into account. In this case, it is convenient to eliminate  $\Psi$  in equation (A12) using

$$\nabla p + \rho \nabla \Psi = 0 \quad (\text{B1})$$

(see equation (A22)) to obtain

$$\mathcal{T}(\hat{\xi}, \xi) = \mathcal{S}_T(\hat{\xi}, \xi) + \mathcal{A}_T(\hat{\xi}, \xi) + \left[ \mathcal{A}_T(\xi, \hat{\xi}) \right]^*, \quad (\text{B2})$$

in which the symmetric part  $\mathcal{S}_T$  and the asymmetric part  $\mathcal{A}_T$  are defined by

$$\begin{aligned} \mathcal{S}_T(\hat{\xi}, \xi) &\equiv \int \frac{1}{\Gamma_1 p} p' [\hat{\xi}^*] p' [\xi] dV \\ &\quad - G \iint \left[ \rho(\mathbf{r}_a) \hat{\xi}^*(\mathbf{r}_a) \cdot \nabla_a \right] \left[ \rho(\mathbf{r}_b) \xi(\mathbf{r}_b) \cdot \nabla_b \right] \\ &\quad \times \left( \frac{1}{|\mathbf{r}_a - \mathbf{r}_b|} \right) dV_a dV_b, \end{aligned} \quad (\text{B3})$$

and

$$\mathcal{A}_T(\hat{\xi}, \xi) = -\frac{1}{2} \int (\hat{\xi}^* \cdot \nabla p) \xi \cdot \left( \frac{\nabla p}{\Gamma_1 p} - \frac{\nabla \rho}{\rho} \right) dV. \quad (\text{B4})$$

In equation (B3),  $p'$  means the Eulerian perturbation to the pressure,

$$p'[\xi] = -\Gamma_1 \nabla \cdot \xi - \xi \cdot \nabla p. \quad (\text{B5})$$

For high-order gravity modes, we may neglect  $\mathcal{S}_T$  because the first term corresponds to the potential energy of the acoustic oscillations, and the second term depends on the perturbation to the gravitational potential (Cowling 1941). In order to evaluate  $\mathcal{A}_T$ , we note that  $p$  and  $\rho$  are functions of only  $\Psi$  in uniformly rotating stars (see equation (B1)). We therefore find

$$\mathcal{T}(\xi, \xi) \approx \int \rho |\xi \cdot \mathbf{e}_{\Psi}|^2 \mathcal{N}^2 dV, \quad (\text{B6})$$

in which  $\mathbf{e}_{\Psi}$  and  $\mathcal{N}^2$  are defined by

$$\mathbf{e}_{\Psi} \equiv \frac{\nabla \Psi}{|\nabla \Psi|} \quad (\text{B7})$$

and

$$\mathcal{N}^2 \equiv \frac{|\nabla\Psi|^2}{\rho} \left( -\frac{dp}{d\Psi} \right) \left( \frac{1}{\Gamma_1 p} \frac{dp}{d\Psi} - \frac{1}{\rho} \frac{d\rho}{d\Psi} \right) \approx \frac{1}{\rho} \left( -\frac{\partial p}{\partial r} \right) \left( \frac{1}{\Gamma_1 p} \frac{\partial p}{\partial r} - \frac{1}{\rho} \frac{\partial \rho}{\partial r} \right). \quad (\text{B8})$$

It is obvious that  $\mathcal{N}^2$  reduces to the (squared) Brunt–Väisälä frequency  $N^2$  in spherically symmetric structures. The approximate equality in equation (B8) is because  $\nabla\Psi$  is almost in the radial direction.

### B3 General formula of the glitch signature

In order to describe the analysis precisely, we consider three different equilibrium structures that are very close to each other. The first (structure 0) is the spherically symmetric one without rotation and any glitches. The second (structure r) has a slow uniform rotation, but without any glitches. The third (structure g) rotates at the same rate as the second and has a glitch. We distinguish the variables of these structures by subscripts 0, r and g for the first, second and third structures, respectively. We derive the frequency difference between structures g and r in the following way: we separately compute the difference between structures r and 0 and that between structures g and 0, and then take the difference between the two differences. Although structures g and r are both deformed by the centrifugal force, its effect on the frequencies cancels out in the leading order when their differences between the two structures are computed. We thus obtain

$$\mathcal{T}_1(\xi_0, \xi_0) \approx \int \rho_0 N_0^2 \xi_r^2 |Y_\ell^m|^2 \frac{\Delta\mathcal{N}^2}{N_0^2} dV, \quad (\text{B9})$$

in which  $\Delta\mathcal{N}^2$  is the difference at the same position, defined by

$$\Delta\mathcal{N}^2 = \mathcal{N}_g^2 - \mathcal{N}_r^2. \quad (\text{B10})$$

In equation (B9), the difference in density is neglected because it has a much smaller impact on the induced glitch signature in the frequency (or period) spectrum than that in  $\mathcal{N}^2$ , which depends on the derivative of the density. In addition, we choose to neglect the difference in  $\mathbf{e}_\Psi$  between structures r and g by assuming that  $\Psi$  of structure g ( $\Psi_g$ ) is a function of only  $\Psi_r$ , which implies that  $\nabla\Psi_g$  is in the same direction as  $\nabla\Psi_r$  at every point. After adopting this assumption, we further approximate  $\mathbf{e}_\Psi$  by  $\mathbf{e}_r$  in equation (B9).

Using equation (A58) and the corresponding expression for  $\xi_r$ ,

$$\xi_r \approx -A \left( \frac{\ell(\ell+1)}{\sigma_0 N_0 \rho_0 r^3} \right)^{1/2} \cos \left( \int_{r_{\text{in}}}^r k_r dr - \varphi_{\text{in}} \right), \quad (\text{B11})$$

we obtain from equations (A24) and (B9) the oscillatory component of the difference in the mode period as

$$\Delta P(n, \ell, m) = \sum_{k=0}^{\ell} \hat{a}_{2k}^g(n, \ell) \mathcal{P}_{2k}^{(\ell)}(m), \quad (\text{B12})$$

in which the period a-coefficients  $\hat{a}_{2k}^g$  are defined by

$$\hat{a}_{2k}^g(n, \ell) \equiv \frac{U_{\ell, k} \Pi_{\ell}}{\sqrt{\ell(\ell+1)} \pi} \int_G \frac{\Delta\mathcal{N}_{2k,0}^2}{N_0^2} \cos(2\mathcal{K}) d\mathcal{K}. \quad (\text{B13})$$

Here, we have introduced the following definitions:

$$\Pi_{\ell} \equiv \frac{2\pi^2}{\sqrt{\ell(\ell+1)}} \left( \int_G \frac{N_0}{r} dr \right)^{-1}, \quad (\text{B14})$$

$$\Delta\mathcal{N}_{2k,0}^2(r) \equiv \int_{4\pi} Y_{2k}^0 \Delta\mathcal{N}^2 d\Omega \quad (\text{B15})$$

and

$$\mathcal{K} \equiv \frac{\sqrt{\ell(\ell+1)}}{\sigma_0} \int_{r_{\text{in}}}^r \frac{N_0}{r} dr - \varphi_{\text{in}}. \quad (\text{B16})$$

In equation (B13), we neglect the contribution of the components that depend on the mode period only smoothly, because it should be ascribed to the period difference between structures r and 0. We retain this treatment throughout this section.

### B4 Three types of discontinuity

Equations (B12) and (B13) provide the fundamental formulae that describe the glitch signature in the period spectrum of high-order gravity modes. The signature depends on the type of discontinuity in  $\Delta\mathcal{N}^2$ . In the following, we consider three different types, which are located at  $r = r_*$  inside the gravity-mode cavity (see Miglio et al. 2008). The corresponding expressions for  $\hat{a}_{2k}^g$  are derived as functions of the mode period  $P_0$  in each case.

If the density itself is discontinuous,  $\Delta\mathcal{N}^2$  follows a Dirac delta function ( $\delta$ ) as

$$\frac{\Delta\mathcal{N}_{2k,0}^2}{N_0^2} = \mathfrak{D}_k^{(0)} r_* \delta(r - r_*), \quad (\text{B17})$$

in which  $\mathfrak{D}_k^{(0)}$  is a dimensionless constant. Then, the  $\hat{a}_{2k}^g$  is given by

$$\hat{a}_{2k}^g(n, \ell) = \mathfrak{E}_{\ell, k}^{(0)} P_0(n, \ell) \cos \left[ \frac{2\pi P_0(n, \ell)}{\Pi_{\ell, *}} - 2\varphi_{\text{in}} \right], \quad (\text{B18})$$

where  $\mathfrak{E}_{\ell, k}^{(0)}$  and  $\Pi_{\ell, *}$  are defined by

$$\mathfrak{E}_{\ell, k}^{(0)} \equiv \sqrt{\frac{\ell(\ell+1)}{(4k+1)\pi}} \frac{U_{\ell, k} \Pi_{\ell} N_0(r_*)}{2\pi} \mathfrak{D}_k^{(0)} \quad (\text{B19})$$

and

$$\Pi_{\ell, *} \equiv \frac{2\pi^2}{\sqrt{\ell(\ell+1)}} \left( \int_{r_{\text{in}}}^{r_*} \frac{N_0}{r} dr \right)^{-1}, \quad (\text{B20})$$

respectively.

If the derivative of the density is discontinuous,  $\Delta\mathcal{N}^2$  is described by a Heaviside step function ( $H$ ) with a dimensionless constant  $\mathfrak{D}_k^{(1)}$  as

$$\frac{\Delta\mathcal{N}_{2k,0}^2}{N_0^2} = \mathfrak{D}_k^{(1)} H(r_* - r). \quad (\text{B21})$$

The corresponding  $\hat{a}_{2k}^g$  is provided by

$$\hat{a}_{2k}^g(n, \ell) = \mathfrak{E}_{\ell, k}^{(1)} \sin \left[ \frac{2\pi P_0(n, \ell)}{\Pi_{\ell, *}} - 2\varphi_{\text{in}} \right], \quad (\text{B22})$$

in which  $\mathfrak{E}_{\ell, k}^{(1)}$  is defined by

$$\mathfrak{E}_{\ell, k}^{(1)} = \frac{U_{\ell, k} \Pi_{\ell}}{2\sqrt{(4k+1)\pi}} \mathfrak{D}_k^{(1)}. \quad (\text{B23})$$

In case where the second derivative of the density is discontinuous,  $\Delta\mathcal{N}^2$  has a form of the ramp function with a dimensionless constant  $\mathfrak{D}_k^{(2)}$  as

$$\frac{\Delta\mathcal{N}_{2k,0}^2}{N_0^2} = \begin{cases} \mathfrak{D}_k^{(2)} \left( 1 - \frac{r}{r_*} \right) & \text{for } r \leq r_* , \\ 0 & \text{for } r \geq r_* . \end{cases} \quad (\text{B24})$$



We then obtain

$$\hat{a}_{2k}^g(n, \ell) = \mathfrak{E}_{\ell,k}^{(2)} P_0^{-1}(n, \ell) \cos \left[ \frac{2\pi P_0(n, \ell)}{\Pi_{\ell,*}} - 2\varphi_{\text{in}} \right], \quad (\text{B25})$$

in which  $\mathfrak{E}_{\ell,k}^{(2)}$  is given by

$$\mathfrak{E}_{\ell,k}^{(2)} \equiv -\sqrt{\frac{\pi}{\ell(\ell+1)(4k+1)}} \frac{U_{\ell,k} \Pi_{\ell}}{2N_0(r_*)} \mathfrak{D}_k^{(2)}. \quad (\text{B26})$$

Equations (B18), (B22) and (B25) demonstrate that, for the three types of discontinuity, the  $\hat{a}_{2k}^g$  coefficients depend on the sinusoidal functions of  $P_0$  with the same period  $\Pi_{\ell,*}$ , but that their amplitude follows a linear or constant or reciprocal function of  $P_0$  for the Dirac or Heaviside or ramp type, respectively.

This paper has been typeset from a  $\text{\LaTeX}$  file prepared by the author.